Delft University of Technology

Document Version
Final published version

Licence
CC BY

Citation (APA)
Yuksel, O., Broggi, G., Hartley, R., Maes, V. K., Baumard, T., Dransfeld, C., Gomarasca, S., Singh, D., Caglar, B., & More Authors (2026). Benchmarking and sensitivity analysis of segmentation methods for image-based fiber detection in composites. *Composites Part A: Applied Science and Manufacturing*, *211*, Article 110150. https://doi.org/10.1016/j.compositesa.2026.110150

Important note
To cite this publication, please use the final published version (if applicable). Please check the document version above.

Copyright
In case the licence states "Dutch Copyright Act (Article 25fa)", this publication was made available Green Open Access via the TU Delft Institutional Repository pursuant to Dutch Copyright Act (Article 25fa, the Taverne amendment). This provision does not affect copyright ownership.
Unless copyright is transferred by contract or statute, it remains with the copyright holder.

Sharing and reuse
Other than for strictly personal use, it is not permitted to download, forward or distribute the text or part of it, without the consent of the author(s) and/or copyright holder(s), unless the work is under an open content license such as Creative Commons.

Takedown policy
Please contact us and provide details if you believe this document breaches copyrights.
We will remove access to the work immediately and investigate your claim.

This work is downloaded from Delft University of Technology.

Composites: Part A 211 (2026) 110150

Contents lists available at ScienceDirect

Composites Part A

journal homepage: www.elsevier.com/locate/compositesa

Benchmarking and sensitivity analysis of segmentation methods for image-based fiber detection in composites

Onur Yuksel [a,1], Guillaume Broggi [a,1], Robin Hartley [b], Vincent K. Maes [b], Theo Baumard [c], Christophe Binetruy [d], Anders Bjorholm Dahl [e], Christian Breite [f], Clemens Dransfeld [a], Wouter Grouve [g], Silvia Gomarasca [a], Rui Guo [f], Adrien Le Reun [c], Arthur Levy [c], David May [h], Mahoor Mehdikhani [f], Andrea Miene [h], Lars Pilgaard Mikkelsen [i], Diwakar Singh [a], Yentl Swolfs [f], Elena Syerko [d], James Kratz [b], Baris Caglar [a,*]

[a] *Aerospace Structures and Materials Department, Faculty of Aerospace Engineering, Delft University of Technology, Kluyverweg 1, 2629HS, Delft, The Netherlands*
[b] *Bristol Composites Institute, University of Bristol, Queen's Building, University Walk, BS8 1TR, Bristol, UK*
[c] *Nantes Université, CNRS, Laboratoire de Thermique et Énergie de Nantes, LTeN, UMR 6607, F-44000, Nantes, France*
[d] *Nantes Université, École Centrale de Nantes, CNRS, GeM, UMR 6183, F-44000, Nantes, France*
[e] *Department of Applied Mathematics and Computer Science, Technical University of Denmark, DK-2800, Kgs. Lyngby, Denmark*
[f] *Department of Materials Engineering, KU Leuven, Kasteelpark Arenberg 44 box 2450, 3001, Leuven, Belgium*
[g] *Production Technology, Faculty of Engineering Technology, University of Twente, Drienerlolaan 5, 7522NB, Enschede, The Netherlands*
[h] *Faserinstitut Bremen, Am Biologischen Garten 2 – Geb. IW3, D-28359, Bremen, Germany*
[i] *Department of Wind and Energy Systems, Technical University of Denmark, DK-4000, Roskilde, Denmark*

ARTICLE INFO

Keywords:
Micrograph
Segmentation
Benchmark
Image analysis

ABSTRACT

The accurate characterization of the microstructure of fiber-reinforced polymer composites is crucial for quality control in manufacturing, material design, and robust performance prediction. Most of the characterization methods rely on the analysis of 2D or 3D images. However, the composites community lacks commonly shared best practices and a clear quantitative understanding of how different image processing approaches compare. This work presents a benchmarking exercise on image processing of fiber-reinforced composite materials to address this challenge. Processing three cross-section micrographs, acquired from a single unidirectional composite sample using typical yet distinct imaging protocols, 11 participants from 8 research institutions extracted fiber centroids and radii. The estimated fiber volume fraction (V_f) values for a single cross-section varied between participants from 0.42 to 0.65. The results highlight the sensitivity of different methods to factors like illumination inhomogeneities, pixel density, polishing-related surface defects, and fiber packing. Considering these observations, several best practices for image analysis are identified, providing critical insight into the methods' sensitivities. To promote transparency and community uptake, the benchmark dataset, evaluation scripts, documentation, and algorithms that were open-sourced are made openly available through a dedicated website, paving the way towards more reliable microstructural analysis in composite materials and ultimately more standardized protocols.

1. Introduction

Materials are typically characterized using homogenized bulk properties. In Fiber-Reinforced Polymer Composites (FRPCs), these include the V_f, average ply thickness, void content, and average fiber orientation. These bulk properties can then be used to estimate macroscopic behavior; e.g., elastic properties are often estimated from V_f using homogenization schemes such as the rule of mixtures [1,2]. Despite providing valuable insights, homogenized properties are inadequate for accurately estimating many composite properties. For instance, Vignoli et al. [1] reported an average error over 30 % when comparing the rule of mixtures with 54 experimental datasets for transverse elastic modulus. Moreover, homogenization, by definition, averages the material's microstructural features, thereby discarding information essential to capturing the multiscale complexity of key physical mechanisms, such as localized failure. Predicting failure initiation [3] or stress

* Corresponding author.
E-mail address: b.caglar@tudelft.nl (B. Caglar).
[1] Both authors contributed equally to this work.

https://doi.org/10.1016/j.compositesa.2026.110150
Received 25 April 2026; Received in revised form 18 July 2026; Accepted 29 July 2026
Available online 14 August 2026
1359-835X/© 2026 The Authors. Published by Elsevier Ltd. This is an open access article under the CC BY license (http://creativecommons.org/licenses/by/4.0/).

Glossary

V_f	Fiber volume fraction
ϕ	Fiber defect ratio
CoV	Coefficient of Variation
ECCM	European Conference on Composite Materials
ELWD	Extra-Long Working Distance
FEPA	Federation of European Producers of Abrasives
FFC	Flat-Field Correction
FPCM	International Conference on Flow Processes in Composite Materials
FRPC	Fiber-Reinforced Polymer Composite
ICC	Intraclass Correlation Coefficient
LCM	Liquid Composite Moulding
LM-PAEK	Low-Melt PolyAryl Ether Ketone
ML	Machine-Learning
Q-Q	Quantile-Quantile
ROI	Region of Interest
RVE	Representative Volume Element
SEM	Scanning Electron Microscopy
SRVE	Statistical Representative Volume Element
TIFF	Tagged Image File Format

concentration around fiber breaks [4], for instance, requires detailed knowledge of the local fiber distribution, which cannot be inferred solely from bulk averages such as the overall V_f.

In recent years, the composites research community has increasingly turned towards micro- and meso-scale analyses to bridge this gap. For this purpose, numerous studies have investigated the microstructural characteristics of composite structures produced with different techniques, such as resin transfer moulding [5,6], vacuum infusion [7], pultrusion [8–10], autoclave processing [11], automated fiber placement [12], or 3D printing [13,14]. In addition, analysis of the raw materials also received considerable attention in the community, including dry fabrics for Liquid Composite Moulding (LCM) techniques or prepregs as semi-products for autoclave or out-of-autoclave processing [15,16]. Their characterization is critical for quality assessment and influences downstream manufacturing processes.

Accurate and consistent microstructural analysis is critical in quality assessment and property prediction of composite materials. Studies have demonstrated that incorporating detailed microstructural information can significantly enhance the accuracy of property predictions [17–19]. Metrics such as the local V_f, local fiber orientation [20,21], first-neighbor distance, fiber misalignment and waviness [22], yarn cross-section geometry, and porosity [23] may be captured by statistical descriptors, which can then be employed to generate realistic virtual microstructures [11,24–27]. Such approaches have been shown to improve the prediction of key properties, including permeability [10], mechanical strength [28,29], fatigue resistance [28–30], or structural battery energy density [31]. Furthermore, the representativeness of these statistical descriptors and virtual microstructures is pivotal to the emerging applications of Machine-Learning (ML) techniques to composite materials [32,33].

To access this level of detail, researchers commonly employ micrographical and tomographical techniques to characterize the internal structure of composite materials. These techniques, which include both 2D imaging (e.g., optical [34], Scanning Electron Microscopy (SEM) [30]) and 3D modalities (e.g., X-ray computed tomography [16,32,35–39]), generate large volumes of visual data that require robust, reliable image processing tools. As imaging technologies evolve, the resolution, speed, and affordability of microstructural characterization have improved dramatically, enabling more widespread use of image-based analyses in academic and industrial settings.

Despite these advances and evidence that image-based analysis can achieve accuracy comparable to particle-sizing methods such as laser diffraction [40], the composites community lacks a standardized framework for evaluating the performance of the image analysis algorithms employed. There is currently little consensus on best practices for extracting microstructural features, leading to inconsistencies between research groups and difficulties in replicating results. Moreover, early-stage researchers and practitioners may struggle to navigate the range of available tools and techniques, potentially leading to misinterpretations or errors in structural characterization. For instance, Sharma et al. [20] reported up to 37 % variation on the estimated elastic modulus depending on the fiber segmentation approach. Hence, preliminary discussions began at FPCM15 and led to an introductory presentation at ECCM21 [41] aimed at highlighting the problem and fostering a shared understanding within the community. These activities ultimately led to a benchmark exercise among 8 European research groups and 11 methods, the results of which are presented in this paper.

The present comparative work analyzes fiber detection algorithms developed or employed by research groups for their accuracy and sensitivity to global image characteristics, such as luminance variation, as well as to local variations arising from broken, touching, or angled fibers. To that end, three cross-sectional micrographs were acquired from a unidirectional Low-Melt PolyAryl Ether Ketone (LM-PAEK) FRPC using different methods to achieve varying pixel densities and illumination conditions. Subsequently, the micrographs were distributed to the participants, who were asked to report the centers and diameters of the detected fibers. No specific constraints on image processing software or techniques were imposed on the participants, and images were analyzed in a blind format using in-house algorithms and methods.

The resulting datasets were compared using various statistical approaches to assess the variability in the captured microstructures. These findings are discussed comprehensively, providing novel insights into the strengths and limitations of different methods, and laying the groundwork for future benchmarking activities. To promote transparency and community uptake, the benchmark dataset was open-sourced and made available from Zenodo [42]. The evaluation scripts, documentation, and algorithms that were open-sourced were also made openly available through a dedicated website [43].

2. Methodology

2.1. Sample preparation and dataset generation

This study was restricted to a unidirectional laminate to simplify the interpretation of results. It was fabricated from a T700G fiber-reinforced LM-PAEK unidirectional prepreg system (TC1225; Toray Advanced Composites). The prepreg, supplied in 12 inch rolls, was cut and stacked in a $[0]_{16}$ layup to form a 300 mm × 300 mm unidirectional laminate. The fiber and prepreg datasheets report a nominal fiber diameter of 7 μm and a matrix weight fraction of 34 %. Consolidation was conducted using a hot press (JOOS Press, United States), by heating to 380 °C at a rate of $2\,°C \cdot min^{-1}$, holding at this temperature for 30 min, then cooling to room temperature at a rate of $2\,°C \cdot min^{-1}$. A constant pressure of 1 MPa was applied throughout the consolidation process.

The sample region was cut from the middle section of the laminate, embedded in clear epoxy, and polished using a Tegramin polishing machine (Struers, Denmark). The grinding step, i.e., initial polishing, was achieved with papers ranging from FEPA P500 to FEPA P4000 (Struers, Denmark). The subsequent polishing operation used two different Dur polishing cloths (Struers, Denmark) with diamond suspensions of 3 μm and 1 μm particle size.

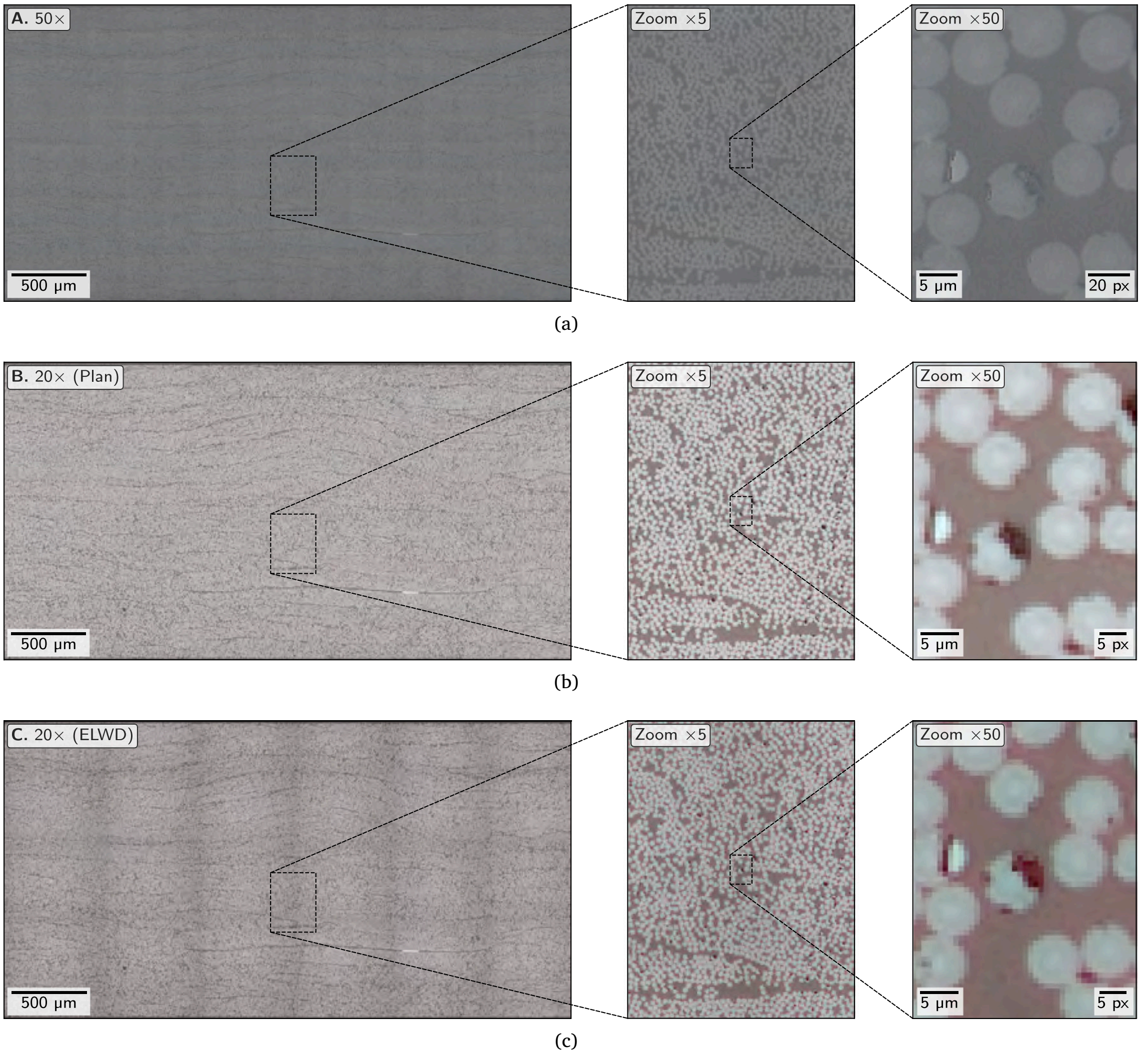

Fig. 1. RGB stitched micrographs and arbitrary zoomed-in snippets: (a) the 50× magnification image; (b) the 20× (Plan) magnification image; and (c) the 20× (ELWD) magnification image. Note that the micrographs were exported at 600 dpi using the nearest interpolation scheme. See [42] for the raw images.

A VK-X1000 confocal microscope (Keyence, Japan) was employed to capture images. A cross-sectional area of $3.8\,\mathrm{mm} \times 2\,\mathrm{mm}$ was scanned by taking successive pictures, or subframes, over a regular grid. The images were then manually stitched using ImageJ (Fiji) [44]. Three distinctive acquisition conditions were achieved by setting three objectives with the same polished cross-sectional area. The first micrograph was captured with an objective at a working distance of 1.1 mm, yielding a 50× magnification. The second micrograph used an objective (Plan) with 20× magnification and a working distance of 3.1 mm. The third micrograph employed an ELWD objective with 11.0 mm working distance, also providing 20× magnification. The higher magnification image boasts a pixel density of $3615\,\mathrm{px} \cdot \mathrm{mm}^{-1}$, or $0.277\,\mu\mathrm{m} \cdot \mathrm{px}^{-1}$, i.e., above the setup resolution of $10\ (3\sigma : 65)\,\mathrm{nm}$; the low-magnification images have a pixel density of $1446\,\mathrm{px} \cdot \mathrm{mm}^{-1}$, or $0.692\,\mu\mathrm{m} \cdot \mathrm{px}^{-1}$. These different procedures were considered representative of sample preparation and image acquisition approaches used worldwide and provide distinct analysis conditions. See [45] for further discussion about sample preparation and image acquisition.

Each micrograph exhibits distinct characteristics and artifacts as shown in Fig. 1. In addition, the acquisition methods introduce variability in pixel intensity distributions and illumination across the micrographs, as shown in Figs. 2(a) and 2(b), respectively. For instance, the 20× (ELWD) images exhibit a significant shading gradient in the transverse direction, resulting in a distinctive illumination pattern after stitching. Note also the presence of a large off-axis fiber in the lower-right quadrant of the micrograph. It only affected a small portion of the micrograph, and its effect will not be discussed in this work. While these variations can be corrected [48–51], the micrographs were distributed to the partners as 32-bit RGB TIFF files without further editing.

2.2. Micrograph analysis methods

A total of 11 research groups from 8 institutions contributed results to this study, see Table S1. The contributions were anonymized and randomly numbered from 1 to 11 prior to analysis. Each participant was asked to process the provided micrographs using their preferred method to obtain a list of fiber centroids and radii. These methods are summarized in Table 1, where their processing steps are grouped according to a common high-level methodological approach followed by all participants (see section S1 for more details). However, the implementations differed: participants used distinct algorithms, and the sequence of processing steps varied between implementations.

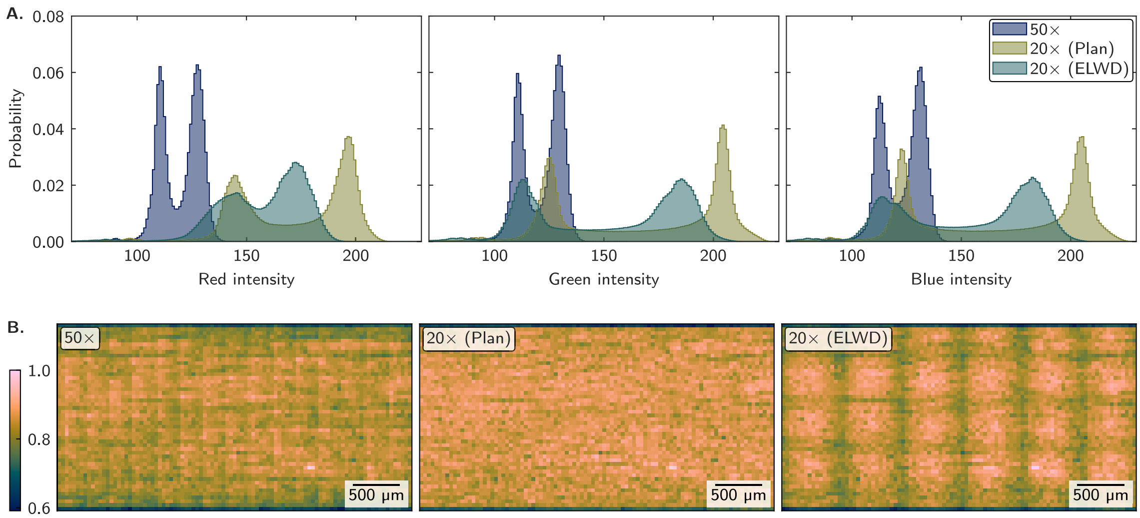

Fig. 2. (a) Pixel intensity distributions across red, green, and blue channels; and (b) grayscale pixel intensity (obtained by weighting the RGB channels following Rec. 601 [46] as implemented in Pillow [47]) normalized by max intensity (95×50 grid). Note the spatial pixel intensity variation caused by uneven illumination (or shading) across the stitched subframes.

First, the raw micrographs were pre-processed to prepare them for further analysis. This stage included steps such as channel reduction (e.g., grayscale conversion), resolution adjustments (e.g., upscaling), denoising (e.g., Gaussian or median filtering), image cleaning (e.g., masking undesired features), and Flat-Field Correction (FFC). Next, most participants segmented the conditioned images to separate fibers from the matrix background (void-free micrographs) and obtain a fiber mask. This step was optionally followed by a labeling step to cluster pixels into individual fibers. Finally, fiber extraction was performed, typically by fitting circles or ellipses on the fiber mask. Some methodologies included post-processing algorithms to, for instance, enforce non-overlapping constraints. Almost all the reported algorithms involved manual steps or manual inputs.

Steps were described at a high level; for instance, there are different conventions for reducing RGB channels to grayscale, and the exact implementation may vary between algorithms. Some participants provided these details in section S1. Depending on the specific algorithm, some steps may also be omitted or applied in a different order. In this work, the order of operations was not explicitly investigated. Assessing such effects would require additional data and dedicated ablation studies in which individual operations are systematically omitted, replaced, or reordered to quantify their impact on the reported metrics. This was outside the scope of the present study and left for future work. Finally, the categorization was partly arbitrary, and a given algorithm can implement multiple conceptual steps. For instance, a denoising operator may also remove small artifacts. The results were collected and post-processed following the methodology detailed in Section 2.3.

2.3. Result analysis methods

In composite material applications, micrograph analysis serves to quantify microstructural characteristics, such as V_f, which may be described at the microscale, typically as a distribution, or homogenized to the meso- or macroscale. In this study, microscale refers to the fiber scale, macroscale to the micrograph (or image) scale, and mesoscale to the in-between scales. Comparative and qualitative performance metrics were employed to evaluate the proposed algorithms and to identify the factors contributing to observed differences in their outcomes. These metrics are overviewed in Table 2. The objective was not to establish an algorithmic ranking, but rather to identify effective practices and formulate methodological guidelines. All the reported analyses were performed in 2D, and the usual terminology of composite manufacturing is employed as appropriate.

2.3.1. Human expert-annotated reference

An expert-annotated reference was established by splitting the images into 20×20 subframes of $190\,\mu m \times 100\,\mu m$ each. The subframe with the highest disagreement in estimated V_f among participants and across micrographs was selected (row 11, column 17). This subframe was manually annotated by three domain experts, each from a different participant. The methodology used to annotate the subframe and aggregate the results is reported in S4.

It is worth noting that this annotation is not intended to represent a ground truth. Fiber boundary identification in micrographs depends on subjective judgment, and different experts may produce different annotations. The expert-labeled subframe is therefore used only as a reference to contextualize the range of results obtained from the automated methods; it is not used to rank or validate the participants' approaches. Using more annotations from the participants does not guarantee a reliable ground truth, as inter-observer variability plays a critical role. Instead, the annotator bias should be quantified in a dedicated study [66].

Microscale descriptive statistics were computed from the labeled fibers and compared with the participants' results. Annotated fibers were then matched to participants' detected fibers using each consensus radius as a proximity criterion, as illustrated in Figure S11. This process enabled a fiber-to-fiber comparison to identify correlations between micrograph features and participant-level trends. The total number of unmatched fibers (i.e, a labeled fiber had no corresponding fiber in the reported results) and multi-matched fibers (i.e, a labeled fiber had multiple corresponding fibers in the reported results) were reported. When multiple fibers were matched, the one nearest to the annotated center was retained for subsequent analysis.

2.3.2. Macroscale descriptive statistics

The outputs of the algorithms were analyzed by calculating statistical descriptors over complete micrographs containing Region of Interests (ROIs). As illustrated in Fig. 3(b), the homogenized V_f was obtained by considering all fibers whose centers lay within a distance equal to the maximum fiber radius from the ROI boundary. Then, the

Table 1
Summary of contributions. Rows summarize each participant's methodology, listing the algorithms used. The same algorithm name may correspond to different implementations, ranging from direct reference versions to in-house optimized procedures. See supplementary section S1 for details.

	Pre-processing				Segmentation	Labeling	Fiber extraction	Post-processing	Refs.
	Upscaling[a]	Artifacts removal[b]	Denoising	FFC					
1	Yes	Masking[c]	No	Gaussian flat-field[c]	No	No	Hough transform	No	[52]
2	No	Morphological closing	No	Normalization	Weka classifier	Watershed	Ellipse fitting	No	[53]
3	No	Morphological closing[c]	No	No[d]	Niblack threshold	No	Ellipse fitting[c]	No	[44,54]
4	Training of three independent networks (include data labeling[c])				InSegt	Watershed	Circle fitting	Remove overlap, adjust position	[55]
5	No	No	Median filter	No	No	No	Hough transform	Remove overlap	[56]
6	Training of three independent networks (include data labeling[c] and augmentation)				U-Net-id	No	Image moment	Remove small features	[57,58]
7	Yes	Morphological closing	Median filter	No	Adaptive threshold[c]	No	Distance transform	Remove overlap	–
8	No	Morphological closing	No	No	Thresholding[c]	No	Laplacian of Gaussian filter[c]	Fixed radius	[44,59, 60]
9	No	Blob analysis	Gaussian bilateral[c] and unsharp masking filters	No	Landini threshold	Watershed	Circle fitting	Fiber merging and re-labeling	[61,62]
10	Yes[a]	No	No	No	No	No	Hough transform[c]	Remove overlapping	[52]
11	No	No	Mean shift filter and Gaussian blur	No	Otsu thresholding	Watershed	Circle fitting, four-direction radius	Remove small and large radii[c]	[63–65]

[a] For 20× magnifications.
[b] Excluding the large off-axis fiber present in the micrograph.
[c] Manual operation or manual parameters.
[d] Using green channel for better contrast.

Table 2
Metrics employed to analyze the participant contributions.

Metric	Scale	Method	Results
Homogenized V_f	Macro	Accounting for overlapping as in Fig. 3(a)	Tab. S3
Homogenized V_f	Macro	Not accounting for overlapping as in Fig. 3(b)	Tab. S4
Fiber count	Macro	–	Tab. S5
Homogenized radius	Macro	–	Tab. S6
Homogenized V_f map	Meso	V_f homogenized over a 20×20 grid	Figs. S2, S4 and S6
Radius distribution	Micro		Fig. 7
Local V_f map	Micro	Voronoïtesselation as in Fig. 4	Figs. S20 to S22
Local V_f distribution	Micro		Fig. 9
First-neighbor distance distribution	Micro	Boundary-to-boundary distance as in Fig. 4	Fig. 10
Average metrics vs. shading	Meso	Shading extracted as in Appendix A	Figs. 11, S23 and S24
Radius error–local V_f correlation	Micro	Eq. (1) applied on fibers matched as in Fig. S11	Tab. S12 and Figs. S25 to S27
Radius error–ϕ correlation	Micro		Tab. S12 and Figs. S28 to S30
Position error–local V_f correlation	Micro	Eq. (2) applied on fibers matched as in Fig. S11	Tab. S12 and Figs. S31 to S33
Position error–ϕ correlation	Micro		Tab. S12 and Figs. S34 to S36

area contribution of each fiber was summed and divided by the ROI area. However, some algorithms may report overlapping fiber areas, which can arise from excessively large fiber diameters or false positives. To characterize this effect, a corrected V_f was obtained by considering the union of the fibers, as shown in Fig. 3(a).

2.3.3. *Microscale descriptive statistics*

At the microscale, the metrics shown in Fig. 4 were used to determine distributions and compare them across participants. The local V_f calculation involves a Voronoi (or Dirichlet) tessellation [67,68]. This method associates each fiber center with a Voronoi cell, which consists of the points in the 2D plane closest to it. It is commonly used in composite materials [69,70] and is a suitable approach when the fiber radii are in a narrow range, while the weighted Laguerre tessellation formulation might better capture larger particle variations as reported for other materials [71]. The local V_f was then defined for each fiber as the fiber area over the area of its Voronoi cell. Note that this approach may produce V_f values greater than 1, e.g., in the case of overlapping fibers or the case of significant mismatch in fiber radii.

Another metric of interest is the nearest-neighbor distance that is known to be influential on microscale flow between fibers [72,73] and crack initiation [74,75]. It is therefore an essential metric for reproducing realistic microstructures [70,76]. This study defines this distance as the span between a fiber boundary and its closest fiber boundary as depicted in Fig. 4. A negative value indicates overlapping fibers.

2.3.4. *Sensitivity and robustness of fiber-detection algorithm*

Algorithmic sensitivity to acquisition, sample preparation, and microstructural factors were assessed. The factors considered were magnification, illumination, polishing-induced fiber damage, and local fiber-packing density. Pairwise Pearson correlations were reported when the results could be linearly related to continuous factors, for instance,

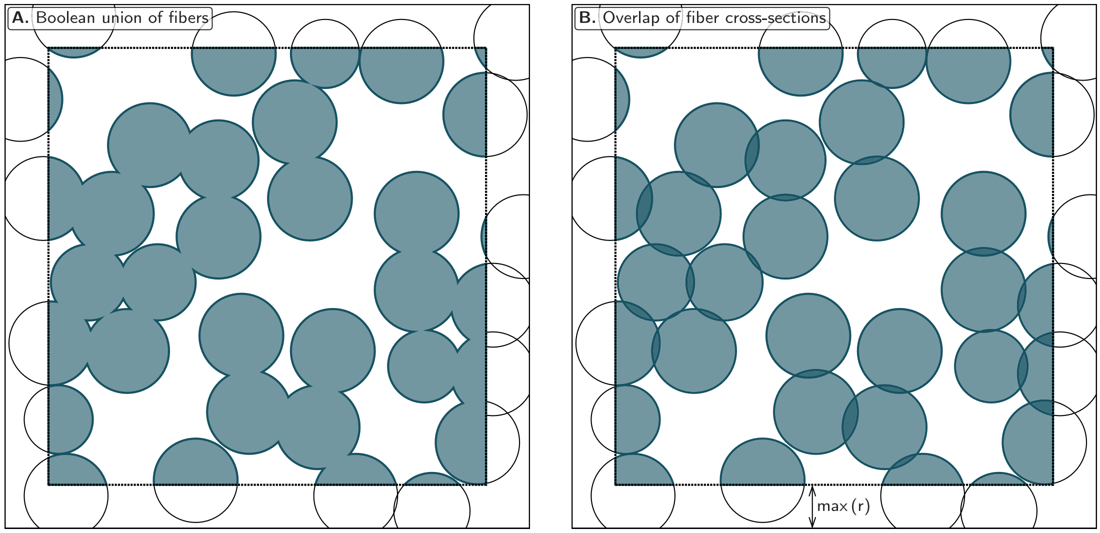

Fig. 3. V_f calculation over a ROI: (a) using the boolean union of fiber surfaces; and (b) using overlaping fiber surfaces. r is the fiber radius.

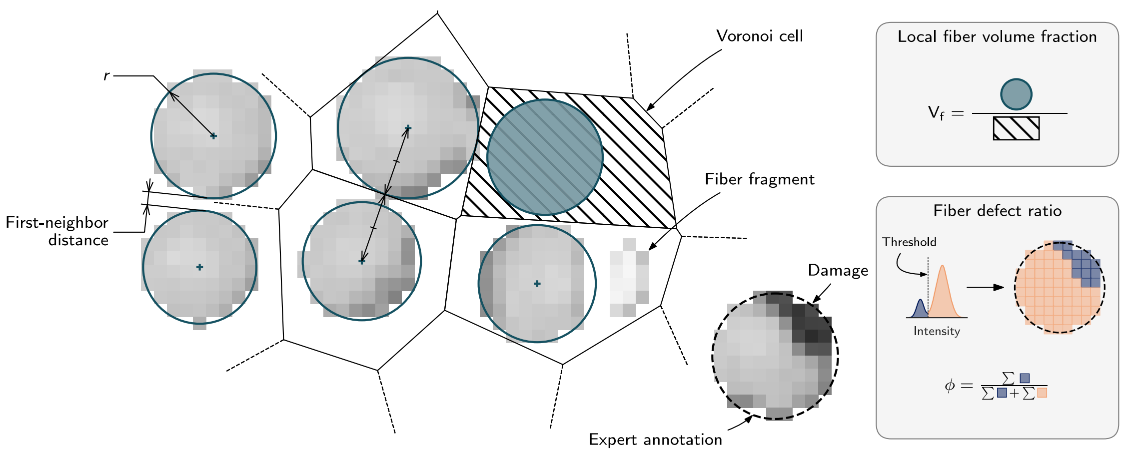

Fig. 4. Schematic representation of the microscale metrics used in this study. The Voronoi cell methodology bounds the surface around fibers and enables the quantification of local metrics.

through the fiber matching procedure described in Section 2.3.1. In that case, significance was assessed with two-sided tests.

As highlighted in Figs. 1 and 2(b), each micrograph exhibited a specific shading pattern that can influence the output of the algorithms. The micrographs were corrected following the methodology detailed in Appendix A to quantify this effect. Then, the background shading was extracted by comparing the original micrograph with the corrected one. The shading was averaged, and its variation was matched with the variation of average V_f, average radius, and average fiber count.

Two metrics were derived from fiber matching results: the error made on fiber radius, see Eq. (1), where r_{expert} and $r_{detected}$ are the radii of the expert-annotated fiber and the detected fiber, respectively; and the error made on fiber position, see Eq. (2), where (x_{expert}, y_{expert}) and $(x_{detected}, y_{detected})$ are the center coordinates of the expert-annotated fiber and the detected fiber, respectively. Note that the position error is absolute and can only be positively correlated. Errors were computed for all matched fibers, and their distributions were correlated with the Voronoi-based V_f calculated as in Fig. 4. This analysis provided information about the influence of fiber packing on both radius and positional errors.

$$r_{error} = \frac{r_{detected} - r_{expert}}{r_{expert}} \tag{1}$$

$$p_{error} = \sqrt{\left(x_{expert} - x_{detected}\right)^2 + \left(y_{expert} - y_{detected}\right)^2} \tag{2}$$

In addition, the influence of fiber damage on detection performance was assessed. Damage extent in polished fibers, referred to as fiber defect ratio (ϕ), appears as dark areas in the micrographs. It was quantified per matched fiber by applying an intensity threshold to the manually labeled fiber pixels. The threshold values were image dependent and equal in the 8-bit grayscale intensity to 115, 166 and 153 for 50×, 20× (Plan), and 20× (ELWD) images, respectively. Then, dark pixels below these threshold values were considered damaged, and ϕ was calculated as the sum of damaged pixels over the sum of all the fiber pixels, as detailed in Fig. 4. ϕ was finally correlated with the position and radius errors.

3. Results and discussion

Fig. 5 shows an arbitrarily chosen subframe for 20× (ELWD) magnification with the detected fibers for each participant. A qualitative visual inspection reveals significant scattering in fiber positions and radii for undamaged fibers, which is further exacerbated in a damaged fiber located near the center of the figure. The lack of robustness of the image processing algorithms was identified as a common shortcoming in Section 3.4.

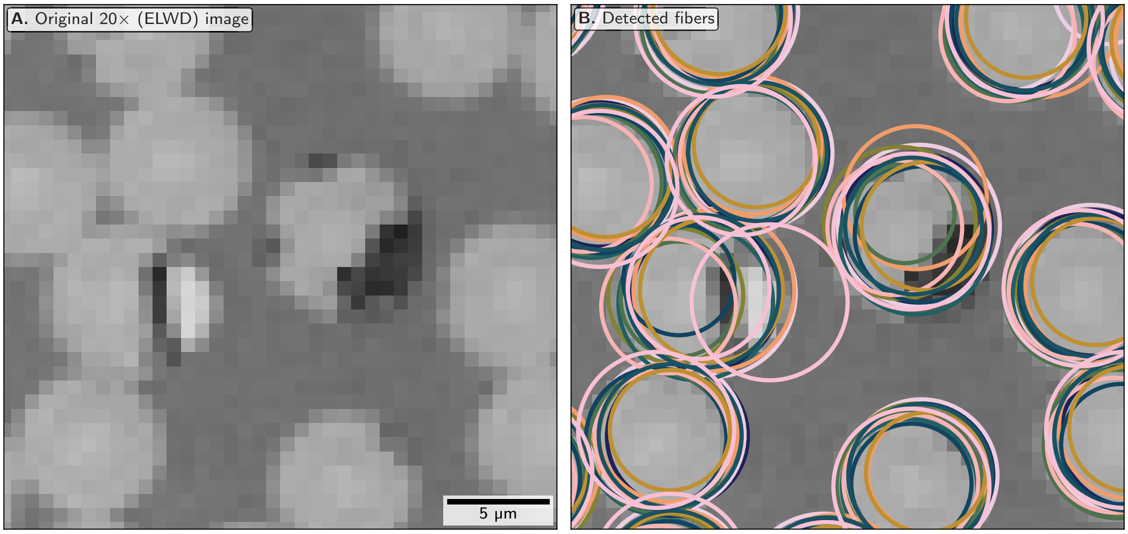

Fig. 5. Inspection of an arbitrarily zoomed-in snippet for 20× (ELWD) magnification: (a) original image and (b) detected fibers where each color denotes a different participant. At this magnification, observations are anecdotal and not representative; the legend is therefore omitted.

Table 3
Unmatched and multi-matched fiber count for each participant, see Section 2.3.1.

	Unmatched											Multi-matched										
	1	2	3	4	5	6	7	8	9	10	11	1	2	3	4	5	6	7	8	9	10	11
50×	0	4	1	1	0	0	5	0	0	0	0	0	0	0	0	0	0	0	1	0	0	2
20× (Plan)	1	6	3	1	5	6	6	4	1	1	7	1	0	0	1	0	0	0	1	0	0	0
20× (ELWD)	1	5	3	2	11	3	5	4	1	3	11	2	0	0	0	0	0	0	0	0	0	0

3.1. Human expert-annotated reference

The expert-annotated reference provided essential insight into why and how algorithms perform differently. It resulted in 252, 255, and 246 labeled fibers by all three experts for 50×, 20× (Plan), and 20× (ELWD) magnifications, respectively. The count difference did not stem from variations in fiber content but from the expert's labeling choices, especially regarding fibers located at subframe edges, and did not affect subsequent analyses. The manual annotation of each subframe required approximately 1 h of human effort, arguably significantly longer than the processing time of any proposed method.

The annotations of each annotator and the consensus are presented in Figures S8 to S10. The extent of agreement for the center coordinates was slightly better than that of radii, and discussed in Section S4.

The expert-annotated reference was compared with the participants' results. Table 3 reports the total number of unmatched and multi-matched fibers per participant, following the methodology detailed in Section 2.3.1. At 50×, only four participants missed fibers, and only two detected multiple fibers for a given expert-annotated fiber. The number of unmatched fibers increased significantly at 20× magnification, with up to 11 occurrences for participants 5 and 11 (about 4 % to 5 % of annotated fibers). While algorithms were generally robust for multi-matching, only participants 1 and 9 missed at most one fiber at any magnification. Participant 9 implemented a post-processing step to identify broken fibers and clumps to merge them or split them, while participant 1 did not post-process the labeled fibers.

3.2. Macroscale descriptive statistics

Fig. 6 exhibits the macroscale statistics calculated for each participant and each micrograph. Fig. 6(a) shows macroscale, i.e, homogenized, V_f calculated from the participant position and radius data, and accounting for fiber overlapping using the method reported in Fig. 3(a). The low-fiber-density laminate edges at the top and bottom of the images were not excluded because they were small relative to the micrograph size and therefore did not significantly influence the results. Each participant, using a different algorithm (refer to Table 1), estimated a V_f ranging from 0.42 to 0.65 across the three source images.

As shown in Fig. 6(c), the micrographs contain more than 1×10^5 fibers, with a Coefficient of Variation (CoV) of 1 % at most and almost no variations among participants and micrographs, except for participants 5 and 11. Hence, the reported scattering in V_f derives from the differences in image-analysis methods and their effect on fiber radii rather than the fiber count. The reported scattering in V_f is significant; for example, applying a rule of mixture [1] to these results would lead to more than 20 % uncertainty in the longitudinal tensile modulus, highlighting the need for a standardized framework.

Fig. 6(d) reports the average fiber radius which ranged from 2.98 μm to 3.71 μm, with CoV of 3 %, 5 %, and 7 % for 50×, 20× (Plan), and 20× (ELWD) magnifications, respectively. The results confirm that the observed V_f scattering is explained by fiber radius scattering, considering the negligible differences in fiber count. For instance, participants 7 and 9 reported the smallest fiber radii as well as the lowest V_f.

Overall, the different methodologies resulted in higher V_f for most participants and better agreement at 50× magnification. The CoV was 6 % for that case; while it was 10 % and 12 % for the two 20× magnification images. Not accounting for fiber overlapping, as reported in Fig. 6(b), did not change the observed trends, and the CoVs remained almost identical, while the average fiber volume increased by 0.01 at most. Overlapping area was insignificant, except for participant 11 who reported values from 2 % to 4 % (see Table S7).

Participants 4, 5, 7, and 10 post-processed overlapping fibers, and 5, 7, and 10 obtained V_f values among the lowest, e.g., an average V_f of 0.48 and average radius of 3.17 μm for participant 7. Participant 4 employed a procedure where fibers were moved and not shrunk to remove overlap (see section S1.4), resulting in higher V_f and radius values. For the other three participants, fiber manipulation may have led to smaller fiber radius measurements, although the underlying

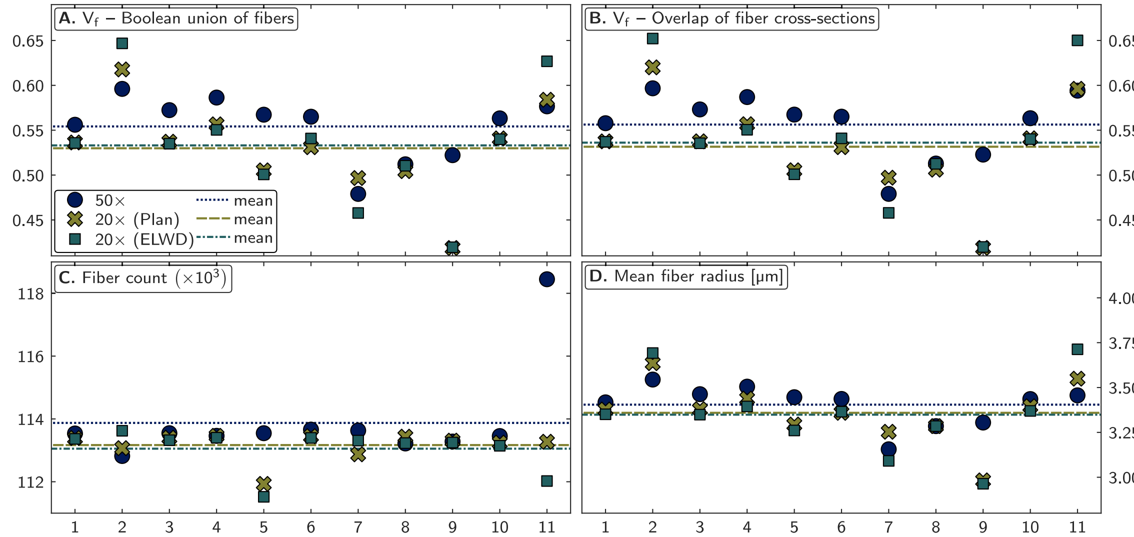

Fig. 6. Macroscale statistics calculated for each participant and each micrograph: (a) V_f using the boolean union of fiber surfaces as in Fig. 3(a); (b) V_f using overlaping fiber surface as in Fig. 3(b); (c) total fiber count; and (d) mean fiber radius. The corresponding values are reported in Tables S3 to S6.

mechanism remains unknown, except for participant 5 who explicitly reported shrinking overlapping fibers (see section S1.5). Nevertheless, participant 9 also obtained low average values, 0.45 for V_f and 3.08 μm for radius, implying other methodological choices may produce the same effects, e.g., the removal of watershed lines (see section S1.9).

3.3. Microscale descriptive statistics

Compared to macroscale descriptors, microscale descriptors provide a more detailed understanding of the material–process–property relationship. However, the intermediate mesoscale is also often of interest for mapping material properties and providing inputs to, for instance, mechanical models. The interested reader is referred to section S3 for a discussion of the results at the mesoscale. In the microscale analysis, the results reported for participants belong to complete micrographs, unless otherwise specified, while the expert annotation results are obtained through the analysis of a subframe.

3.3.1. Radius distributions

Fig. 7 reports the distributions of fiber radii for each participant and each micrograph, and the expert-annotated reference. Overall, they are well approximated in their central regions by normal distributions as discussed in section S5. Additionally, the figure shows the radii measured by Mesquita et al. [40] using a laser diffraction system on T700SC-12 K-50C fibers and approximated by a normal distribution of $\mu = 3.38$ μm and $\sigma = 0.16$ μm (recalculated from the 217 provided data points [77]). This mean radius was found approximately 150 nm lower than those obtained in this work: $\mu = 3.56$ μm and $\sigma = 0.19$ μm, $\mu = 3.53$ μm and $\sigma = 0.18$ μm, $\mu = 3.52$ μm and $\sigma = 0.19$ μm for 50×, 20× (Plan), and 20× (ELWD) magnifications, respectively, as reported in Table S8.

The consistency of distributions for 20× Plan and 20× ELWD magnification and the distinguishably different distributions at the 50× magnification suggest that the image resolution significantly influenced the algorithm outputs, while the working distance of objectives at 20× did not have a significant influence. Participants 3, 4, 5, 9, and 10 had positively shifted distribution for 50× (i.e., larger mean and median radii) and the inverse was observed for participant 2 while participant 1 and 5 reported narrower distributions at the 50× magnification, which can be attributed to the presence of crisper fiber boundaries at high resolution resulting in smaller uncertainty in detected boundaries.

The radius data obtained by participant 6, 7, 8, and 11 resulted in unexpected distributions. The discrete nature of the distributions obtained by participant 6 for the 20× micrographs could be due to a lack of data representativeness when training individual machine-learning networks for each micrograph, although a more continuous distribution was observed for participant 4, who also trained individual networks. The fibers used for training may be too similar in size, potentially leading to overfitting and explaining a discrete output. Participant 8 enforced a constant fiber radius. Finally, the gaps observed in the results provided by participants 7 and 11 may be related to the post-processing they performed based on fiber size and overlapping. For instance, specific radius values may have been excluded.

The results highlight potential radius-dependent biases in segmentation and post-processing. Specifically, non-linear segmentation operations, such as morphological closing (a dilation followed by an erosion), may artificially increase fiber dimensions and lead to an over-representation of large radii, as observed in this work. Some participants noted that circle or ellipse fitting algorithms exhibited a dependence to resolution. In this case, upscaling low-magnification images (as done by participants 1, 7, and 10) appeared to reduce the discrepancy with high-magnification distributions relative compared to cases without upscaling (e.g., participants 5 and 9) when fitting circles or ellipses. However, such upscaling does not increase the amount of intrinsic information.

Finally, the variations observed in Fig. 7 may also have arisen from threshold effects introduced by the finite pixel size that discretizes the continuous radius values. The standard deviation values reported in Table S8 are close to or below the pixel size (0.277 μm and 0.692 μm, refer to Section 2.1), suggesting that the resolution is too coarse to capture the radius variations properly. For instance, participant 9 obtained a mean radius approximately 0.3 μm smaller for the 20× magnifications compared to the 50× one. This difference may be attributed to the watershedding algorithm employed by participant 9, which produced watershed lines subtracted from touching fibers, leading to smaller fibers. The apparent reduction in fiber size was more pronounced in low-magnification micrographs, where watershed lines accounted for a larger proportion of fiber pixels.

This observation also highlights the need for more detailed reporting to properly assess the fitting algorithms, for example, whether fibers are fitted to the internal or external boundaries of the fiber mask. These hypotheses could be tested in future research by simulating the pixelation of ground truth data to evaluate its effect on the algorithms.

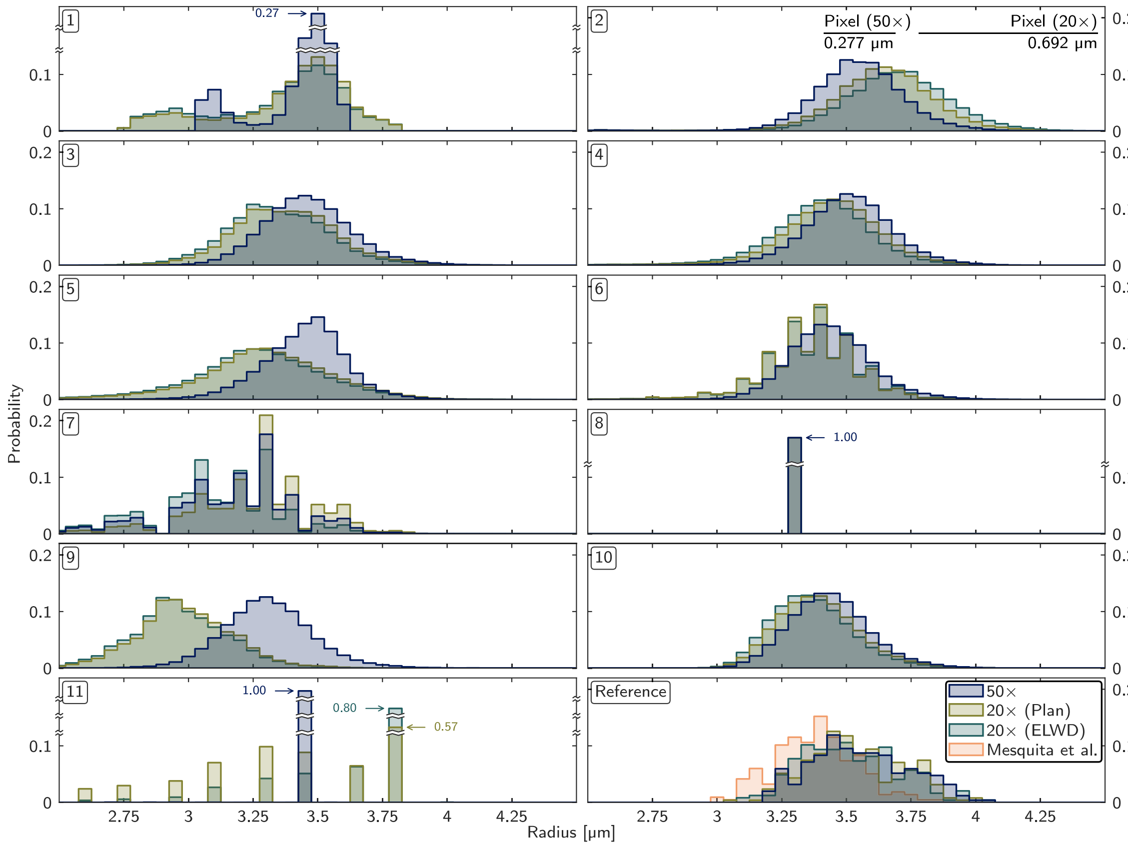

Fig. 7. Distribution of the fiber radii obtained by each participant for 50×, 20× (Plan), and 20× (ELWD) images. The reference distributions include results from the expert-annotated reference and measurements on T700SC-12 K-50C fibers by Mesquita et al. [40]. Bin size is 0.05 μm, probabilities are rounded to the second place, and some axes are broken for readability.

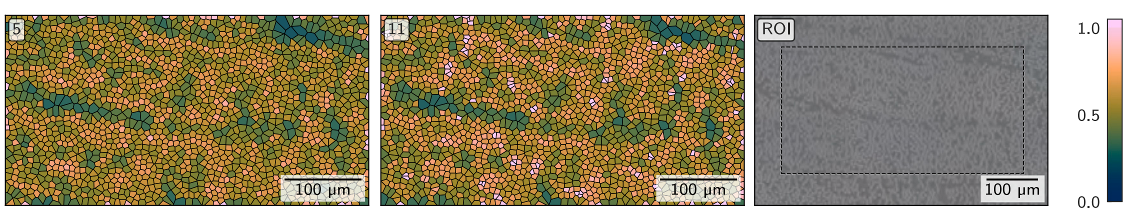

Fig. 8. Overview of the local V_f defined over Voronoi cells for two participants at 50× magnification. A V_f above 1 denotes a fiber that completely overlaps its Voronoi cell. See Figures S20 to S22 for the full set of results.

More broadly, this study could not quantify the causal contribution of each algorithm to the observed variability due to a lack of controlled ablation or factorial experiments. For instance, participants 1, 5, and 10 applied a Hough transform [52] without thresholding or labeling (Table 1) and obtained distinct results which are not explainable without more details.

3.3.2. Local fiber volume fraction distributions

Fig. 8 provides an overview of the Voronoi tessellation for the 50× magnification, presenting two examples that illustrate the variability in local dual-scale microstructure. The remaining tessellations show similar trends, and the full set of results for all participants and magnifications is included in the supplementary information (see Figures S20 to S22). Overall, all algorithms effectively captured a similar local dual-scale microstructure, particularly in resin-rich regions characterized by larger, lower V_f cells. However, the methodology employed by participant 11 yielded many smaller cells in the packed regions, leading to a higher V_f. These could be attributed to the additional fibers reported in Table S5, which also skew statistical descriptors.

The local V_f distributions shown in Fig. 9 exhibited trends similar to the radius distributions, in agreement with the fiber counts that were comparable for all the participants (Fig. 6(c)). As discussed in section S5, they are overall well approximated by normal distributions. Interestingly, the three distributions were alike, regardless of magnification.

The mean and standard deviation of local V_f obtained for the 50× distributions ranged from 0.59 to 0.62 and 0.11 to 0.12, respectively (Table S9). This result agreed with the expert-annotated reference, indicating that the algorithms captured similar characteristics in the distributions' central regions. Participants 7, 8, 9, and 11 were notable exceptions to this observation, with $\mu = 0.50$, 0.53, 0.55 and 0.64, respectively. These results are consistent with the observations for their radius distributions. For participant 8, the discrepancy can be explained by their use of a constant radius of 3.28 μm, which is smaller than

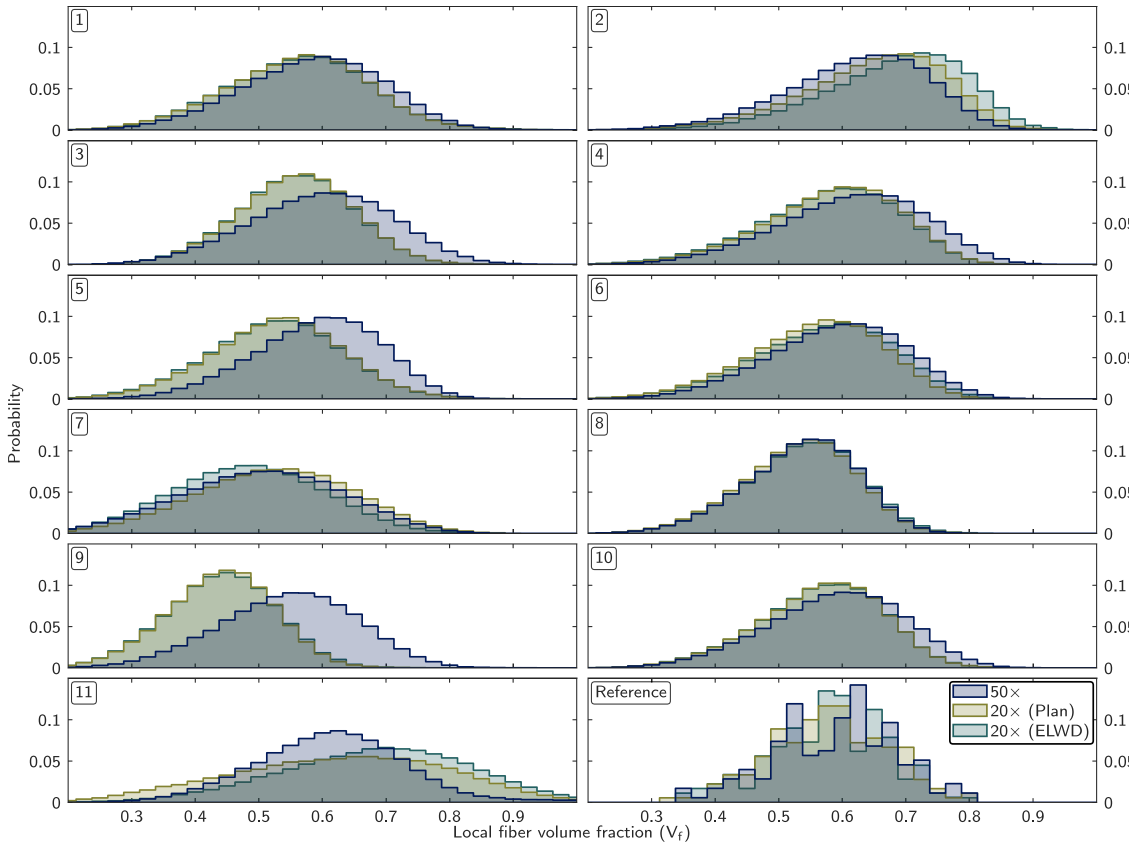

Fig. 9. Distribution of the local V_f for each participant in 50×, 20× (Plan), and 20× (ELWD) images. The reference distributions include the results obtained with the expert-annotated reference. Bin size is 0.025.

the rest of the participants' and the expert-annotated case's radii. The post-processing algorithms used by participants 7 and 9 may also have decreased the mean local V_f. The presence of values significantly above the theoretical limit for participant 11 in Fig. 9 indicated significant overlapping. Finally, the 20× distributions exhibited mean values overall farther from the expert-annotated reference, while the reported standard deviations were comparable, except for participants 9 and 11.

3.3.3. *First-neighbor distance distributions*

Fig. 10 presents the first-neighbor distance distributions. The expert-annotated reference yielded a slightly narrower distribution at 50× magnification, indicating that the image resolution may have played a minor role. These three distributions were approximately centered at 0 μm, with a significant proportion of negative values overlapping, indicating that the manual labeling procedure did not yield physically valid results, since fiber interpenetration is impossible. The amount of overlap was mostly below 0.5 μm, i.e., close to or below the pixel size at both magnification levels. Also, the fibers may not have been perfectly circular [78], and describing them as circles rather than, e.g., ellipses may have led to overlaps when fibers are in contact.

Consistent with the expert-annotated reference, all participants reported overlapping fibers, except 5 and Johnson S_U distributions were fit as reported in section S5. The truncated distribution obtained for participant 5 could be attributed to the post-processing of overlapping fibers (refer to Table 1). However, participants 4, 7, and 10 also post-processed overlapping but reported small negative distances, close or below the pixel size. It suggests that non-overlap may have been enforced at the pixel level (with rounding effects) or that a small tolerance for overlap was allowed.

Interestingly, the results obtained by participant 9 showed larger distances at low magnifications than at high magnifications. This observation was consistent with the smaller radii reported in Fig. 7 for low magnification and further supported the hypothesis that watershed line removal led to smaller radii, smaller V_f, and larger first-neighbor distances in low-magnification images. Finally, participants 1, 7, 8, and 11 showed more dispersed distribution. While no cause was identified for participants 1 and 7, the dispersion may be due to the fixed radius enforced by participant 8. The distribution obtained by participant 11 was unexpected but consistent with this participant's results regarding local V_f and radius distributions. This may indicate an issue with the employed algorithm, and these results should be interpreted with nuance.

3.4. *Sensitivity and robustness of fiber-detection algorithm*

3.4.1. *Shading*

This work reports significant variations in results between the algorithms at both 50× and 20×, some of which may be attributed to shading artifacts. The 50× and 20× ELWD images exhibited highly contrasted shading, corresponding to the border of the stitched individual micrographs. The shading value was averaged over image height and plotted as a function of image width in Fig. 11 for 50× image, where positive shading values indicate darker regions, and compared with the spatial variation of statistical descriptors calculated over the same vertical strips: homogenized V_f, fiber count, and average fiber radius. Some methods exhibited a noticeable correlation between shading variations and V_f, with local minima of V_f coinciding with local extrema in shading. The same analysis is reported in Figures S23 and S24 for 20× (ELWD) and 20× (Plan) magnification, respectively.

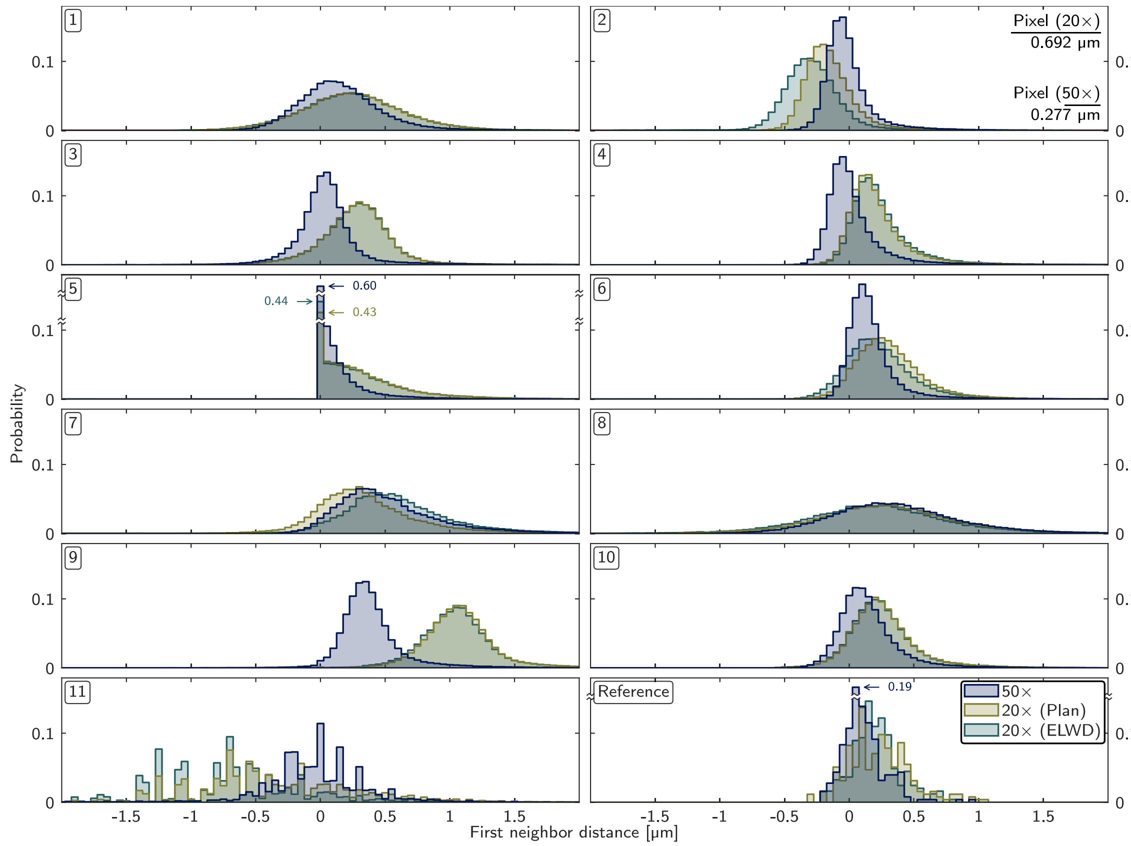

Fig. 10. Distribution of the first neighbor distance for each participant in 50×, 20× (Plan), and 20× (ELWD) images. The reference distributions include the results obtained with the expert-annotated reference. Bin size is 0.05 μm, probabilities are rounded to the second place, and some axes are broken for readability.

More detailed analysis of correlation between shading data and the statistical descriptors using Pearson correlation coefficients is reported in Table S11.

Participants 1, 2, 4, 6, 7, and 9 a negative significant correlation between shading and fiber radius. One possible explanation is that higher fiber density increases the total fiber area within a subframe, potentially reducing apparent shading because fibers appear brighter than the matrix. If this hypothesis were correct, shading should have also correlated with fiber count in individual subframes, because more fibers also increase total fiber area. However, no correlation with fiber count was observed.

These results suggest that shading primarily biased the thresholding algorithms towards smaller radii, thereby reducing the estimated V_f. Similar patterns were observed in the 20× (ELWD) micrograph, where shading was pronounced. In contrast, in the 20× (Plan) micrograph, where shading was weaker, no significant correlation between shading and fiber radius was found; instead, several participants reported a significant negative correlation between shading and fiber count. This observation suggests that the matrix contributed more strongly to the estimated shading in this image.

Nevertheless, these findings do not directly confirm any hypothesis. Future work could test these mechanisms by simulating shading on ground-truth images and assessing the resulting effects on the algorithms.

Participants 3 and 5 reported a weaker correlation between shading and V_f, and no correlation between shading and fiber radius (Table S11). The documented usage of a local, adaptive thresholding for participant 3 (see Table 1) may have reduced the bias from shading. However, adaptive thresholding did not guarantee robustness to shading, as highlighted by the results from participants 7 or 11, although the latter results should be examined with care, given how the radius, local V_f, and first-neighbor distance distributions diverged from the other participants (see Section 3.3). Participant 1 used a flatfield correction to address shading. This approach seems to have been effective in the case of 20× (ELWD) micrograph where no correlation was obtained between shading and fiber radius (Table S11), but not for the 50× magnification. A contributing factor may have been that the Gaussian kernel widths used for flatfield correction were not scaled in strict proportion to the image resolution, as reported in section S1.1. With a density of $3615\,\mathrm{px}^2\cdot\mathrm{mm}^{-1}$ (50× magnification), $\sigma = 100\,\mathrm{px}$ corresponds to $28\,\mu\mathrm{m}$, while at $1446\,\mathrm{px}^2\cdot\mathrm{mm}^{-1}$ (20× magnification), $\sigma = 50\,\mathrm{px}$ corresponds to $35\,\mu\mathrm{m}$. Future research should detail the effect of these algorithms to formulate precise recommendations.

3.4.2. *Local* V_f

Although successive polishing operations can achieve a near-perfect sample surface, defects within the fiber cross-sections are inevitable. These defects and the packing density significantly influence the image processing algorithms, as highlighted in Fig. 5. Comparing the expert-annotated fiber radii and locations with the detected fibers enabled an in-depth analysis. The fiber radius error, the position error, the local V_f, and the defect ratio ϕ were calculated as in Section 2.3.4. The pairwise Pearson coefficient between these metrics is reported in Table S12, and the evolution of these metrics with respect to each other can be visualized in Figures S25 to S36.

All participants, except 7, exhibited a significant, mild, and negative correlation between the error made on radius values and local V_f for all three images, with the effect being prominent for the 50× magnification case. The results were less correlated at higher magnification because the error magnitude decreased as resolution increased, indicating that

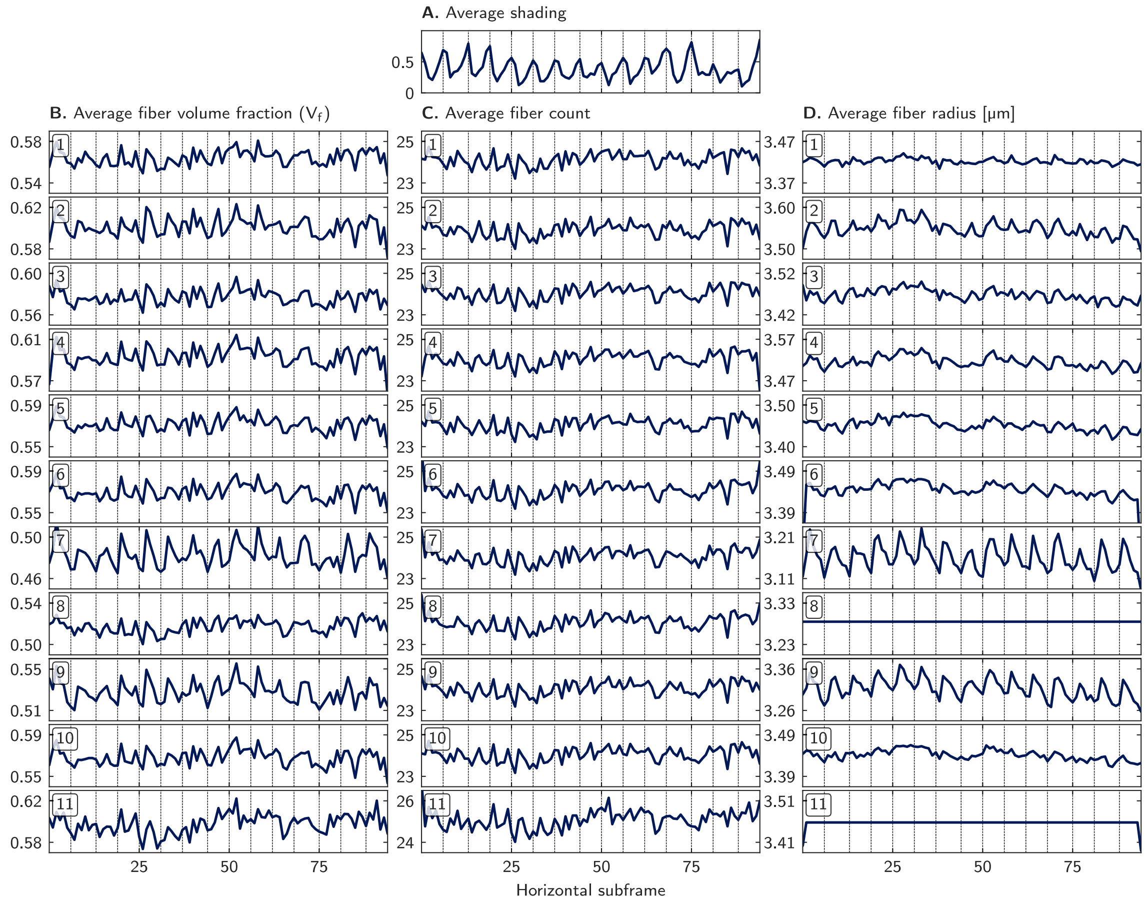

Fig. 11. Average metrics over 95×1 subframes (i.e., along the horizontal axis) for 50× magnification: (a) shading, (b) V_f, (c) fiber count, and (d) fiber radius. Averages were calculated excluding resin-rich borders.

the algorithms produced results that more closely matched the expert-annotated reference. These trends are clearly identifiable in Figures S25 to S27.

The reported negative correlation indicated that algorithms measured smaller radii than the expert-annotated reference as fiber packing increased. The error magnitude was below the pixel size and could be attributed to a bias in the human expert-annotated results. Yet, given that increasing the magnification provided results closer to the reference, it may be concluded that the error was related to the discretization effect caused by the pixel size when processing fibers in contact, as hypothesized in Section 3.3.1.

The error made on the reported fiber positions was not found to be significantly correlated with the local V_f, except for participant 1 in the 20× (Plan) image. However, no cause for this result was identified. These observations suggest that fibers were not displaced when overlapping overall, but only reduced in size.

3.4.3. Damaged fibers

All participants showed a significant, mild-to-strong correlation between fiber-position error and fiber defect ratio(ϕ) in at least one micrograph, if not all. In that case, the error magnitude was often above the pixel size, especially when $\phi > 0.2$. Participants most affected by the sensitivity of fiber position to fiber damage used a circular or elliptical fitting approach to detect fibers. If a segmented fiber is incomplete, a circle or ellipse fit will likely result in a shifted center, especially if the algorithm is biased towards perfect geometries. Conversely, the edge detection method used by participant 4 was less sensitive to ϕ.

The strongest correlations were reported for the 50× micrograph. It suggests that enhanced magnification negatively affected performance in ϕ, highlighting imperfections. These features remain blurred within the fiber body at lower resolution, whereas at higher resolution they may be more readily distinguished and misclassified as separate objects, or they may mislead algorithms. For instance, participant 1 had to fit weaker Hough transform accumulator circles in the 50× image, as documented in section S1.1. Participants 2, 4, 6, 7, 9, and 10 reported results exhibiting a significant and negative correlation between the radius error and the defect ratio ϕ. Nevertheless, the error was below the pixel size.

4. Recommendations

The results obtained in this work demonstrate that the choice and parameterization of processing algorithms, as well as the image-acquisition conditions, such as magnification and illumination, substantially influence composite micrograph segmentation. Consequently, the microstructural descriptors derived from that segmentation are also affected; for example, participants reported up to 12 % CoV on macroscale V_f.

The reported variability is significant, especially given the high quality of the micrographs and the absence of defects such as voids. These findings raise concerns about interpreting results when measurement variability is not discussed, thereby undermining reproducibility. Consequently, this work advocates for community-defined best-practice guidelines.

Based on the statistical analyses performed in this work, we formulate the following evidence-based recommendations were formulated for applying image-based characterization workflows:

- Accounting for shading effects and polishing-induced fiber damage in the image analysis algorithms, through adaptive thresholding or flattening for the former and through opting for edge detection instead of circle fitting for the latter;
- Avoiding post-processing to reduce fiber-overlap unless strictly required, as steps such as watershedding to define overlap boundary are sensitive to pixel size and lead to loss of information;
- Performing and reporting sensitivity or convergence analyses according to the employed algorithms, e.g., sensitivity to threshold values or to smoothing kernel size;
- Systematic reporting of acquisition parameters, algorithms, and their settings, together with the source code and micrographs used for the analysis;
- Use of higher magnification to reduce error and inter-method variability (here, a 50× magnification was found to improve results significantly for a carbon-fiber unidirectional micrograph except for the sensitivity to damaged fibers);
- Critical assessment of results and underlying distributions.

While some of the items in the guideline may seem trivial, the literature often omits such details. Consistent adherence will improve the interpretation of results and facilitate data reuse.

These guidelines are even more important because, in this benchmark exercise, it was impossible to clearly identify which methodological approaches produce the best results under which conditions, since the operation order and ablation study were out of scope. It is worth noting that a more detailed sensitivity analysis is required before generalizing the relative performance of reported approaches. To better understand existing image-based analysis methods and to guide methodological development, future research should:

- Address more representative micrographs, including defects, non-circular fibers, orientation quantification [20], and optimal Statistical Representative Volume Element (SRVE) [18] or Representative Volume Element (RVE) [79];
- Benchmark algorithms against a public dataset, ideally supported by community-recognized ground truths acquired through, e.g., SEM combined with ion beam polishing to avoid fiber damage as in [80];
- When using this dataset, benchmark the results against what is reported here, e.g., to make a more accurate assessment of V_f, which varies between 0.42 and 0.65 in this study.
- Quantify the computational cost of the different algorithms;
- Account for the limitations of homogenized descriptors, which poorly capture inter-method variability;
- Move towards standard procedures, identified through more guided benchmarking activities or by accessing algorithm source codes for detailed parameter variation and ablation studies;
- Explore alternative approaches not considered in this study, such as sub-pixel edge detection algorithms.

5. Conclusion

In this first benchmarking exercise of image-based analysis methods for composite segmentation and microstructure characterization, 8 research groups reported results from 11 state-of-the-art methods applied to three micrographs of the same region of a unidirectional laminate acquired under three different experimental conditions. Participants reported fiber locations and radii. These data were then analyzed to derive microstructural descriptors. Defects such as voids were excluded, and no restrictive guidelines were imposed, allowing each group to apply its usual workflow.

This work compiles and documents state-of-the-art segmentation methods and quantifies the sensitivity of current approaches through an anonymized, blinded evaluation. It demonstrates the significant variability in the results obtained by these methods and proposes guidelines based on statistical analyses.

While this benchmarking paves the way towards standardized protocols in line with recent efforts to improve the reliability of composite material characterization (e.g., for permeability [81–85] and tensile properties [86]), its scope is limited to defect-free unidirectional laminates and a restricted set of descriptors. Moreover, the effect of algorithm parameterization (e.g., threshold values) was not discussed, although such choices may substantially influence material characterization [87].

CRediT authorship contribution statement

Onur Yuksel: Writing – review & editing, Writing – original draft, Software, Project administration, Methodology, Investigation, Formal analysis, Data curation, Conceptualization. **Guillaume Broggi:** Writing – review & editing, Writing – original draft, Software, Project administration, Methodology, Investigation, Formal analysis, Data curation, Conceptualization. **Robin Hartley:** Writing – review & editing, Methodology, Investigation, Conceptualization. **Vincent K. Maes:** Writing – review & editing, Methodology, Investigation, Conceptualization. **Theo Baumard:** Investigation, Conceptualization. **Christophe Binetruy:** Investigation. **Anders Bjorholm Dahl:** Investigation. **Christian Breite:** Investigation. **Clemens Dransfeld:** Investigation. **Wouter Grouve:** Writing – review & editing, Investigation. **Silvia Gomarasca:** Investigation. **Rui Guo:** Investigation. **Adrien Le Reun:** Investigation, Conceptualization. **Arthur Levy:** Writing – review & editing, Investigation, Conceptualization. **David May:** Investigation. **Mahoor Mehdikhani:** Writing – review & editing, Investigation. **Andrea Miene:** Investigation. **Lars Pilgaard Mikkelsen:** Investigation. **Diwakar Singh:** Investigation. **Yentl Swolfs:** Writing – review & editing, Investigation. **Elena Syerko:** Investigation. **James Kratz:** Writing – review & editing, Supervision, Methodology, Conceptualization. **Baris Caglar:** Writing – review & editing, Supervision, Methodology, Conceptualization.

Declaration of generative AI and AI-assisted technologies in the manuscript preparation process

During the preparation of this work, the authors used Grammarly, Le Chat (Mistral AI), and ChatGPT (OpenAI) to enhance language and readability. After using these tools, the authors reviewed and edited the content as needed and take full responsibility for the content of the published article.

Declaration of competing interest

The authors declare that they have no known competing financial interests or personal relationships that could have appeared to influence the work reported in this paper.

Acknowledgments

Figures use the color-vision deficiency-friendly and perceptually-uniform Batlow and Managua colormaps [88]. G. Broggi would like to acknowledge the CAELESTIS project, funded by the European Climate, Infrastructure and Environment Executive Agency (CINEA) under Grant Agreement No. 101056886. R. Guo would like to acknowledge his PhD scholarship from the China Scholarship Council (202006430010). M. Mehdikhani and C. Breite would like to acknowledge FWO Flanders for their FWO postdoc fellowships BIOPTOUGH 12B0624N) and SUBFIRE (12A0625N), respectively.

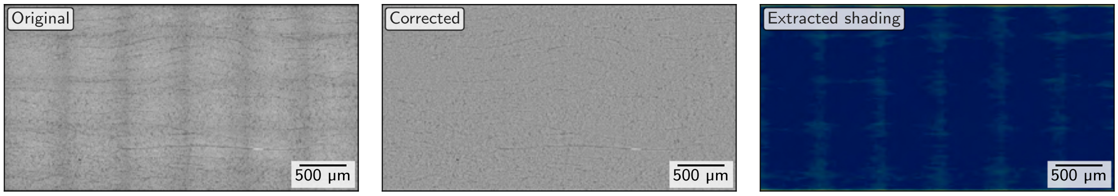

Fig. A.12. Original micrograph, corrected image and shading estimation for the 20× ELWD magnification.

Appendix A. Methodology: shading correction

To correct shading, the micrographs were first converted to grayscale following Rec. 601 [46] as implemented in Pillow [47]. Then, the Python implementation of the BaSiC algorithm [50] was applied with a flatfield smoothness value of 1 and a smoothness deflection value of 5. Refer to the original publication for details on the implementation.

The micrographs corrected by the BaSiC method were finally subtracted from the original micrographs, providing a quantitative estimate of image shading. This process is illustrated in Fig. A.12. The shading measured by this method increased monotonically with pixel darkness.

Appendix B. Supplementary data

Supplementary material related to this article can be found online at https://doi.org/10.1016/j.compositesa.2026.110150.

Data availability

The benchmark dataset was open-sourced and made available from Zenodo [42].

References

[1] Vignoli LL, Savi MA, Pacheco PM, Kalamkarov AL. Comparative analysis of micromechanical models for the elastic composite laminae. Composites B 2019;174:106961. http://dx.doi.org/10.1016/j.compositesb.2019.106961, URL: https://linkinghub.elsevier.com/retrieve/pii/S1359836819313794.

[2] Yu W. Common misconceptions on rules of mixtures for predicting elastic properties of composites. AIAA J 2024;62(5):1982–7. http://dx.doi.org/10.2514/1.J063863, URL: https://arc.aiaa.org/doi/10.2514/1.J063863.

[3] Kohler S, Cugnoni J, Amacher R, Botsis J. Transverse cracking in the bulk and at the free edge of thin-ply composites: Experiments and multi-scale modelling. Composites A 2019;124:105468. http://dx.doi.org/10.1016/j.compositesa.2019.05.036, URL: http://www.sciencedirect.com/science/article/pii/S1359835X19302118.

[4] AhmadvashAghbash S, Fazlali B, Mehdikhani M, Swolfs Y. Finite element analysis of the effect of longitudinal debonding on stress redistributions around fibre breaks in randomly packed fibres. Compos Sci Technol 2022;227:109586. http://dx.doi.org/10.1016/j.compscitech.2022.109586, URL: https://linkinghub.elsevier.com/retrieve/pii/S0266353822003281.

[5] Gommer F, Endruweit A, Long A. Quantification of micro-scale variability in fibre bundles. Composites A 2016;87:131–7. http://dx.doi.org/10.1016/j.compositesa.2016.04.019, URL: https://www.sciencedirect.com/science/article/pii/S1359835X16300951.

[6] Abliz D, Finke B, Berg DC, Schilde C, Ziegmann G. Flow of quasi-spherical nanoparticles in liquid composite molding processes. Part I: Influence of particle size and fiber distance distribution. Composites A 2019;125:105563. http://dx.doi.org/10.1016/j.compositesa.2019.105563, URL: https://www.sciencedirect.com/science/article/pii/S1359835X19303124.

[7] Vilà J, Sket F, Wilde F, Requena G, González C, LLorca J. An in situ investigation of microscopic infusion and void transport during vacuum-assisted infiltration by means of X-ray computed tomography. Compos Sci Technol 2015;119:12–9. http://dx.doi.org/10.1016/j.compscitech.2015.09.016, URL: https://www.sciencedirect.com/science/article/pii/S0266353815300889.

[8] Yuksel O, Sandberg M, Hattel JH, Akkerman R, Baran I. Mesoscale process modeling of a thick pultruded composite with variability in fiber volume fraction. Materials 2021;14(13). http://dx.doi.org/10.3390/ma14133763, URL: https://www.mdpi.com/1996-1944/14/13/3763.

[9] Qi S, Alajarmeh O, Shelley T, Schubel P, Rendle-Short K, Zeng X. Formation of non-uniform fibre distributions in winding-pultrusion process and its effect on axial compressive properties of hollow gfrp profiles. Composites A 2023;173:107659. http://dx.doi.org/10.1016/j.compositesa.2023.107659, URL: https://www.sciencedirect.com/science/article/pii/S1359835X2300235X.

[10] Yuksel O, Caglar B, Broggi G, Michaud V, Akkerman R, Baran I. Saturated transverse permeability of unidirectional rovings for pultrusion: The effect of microstructural evolution through compaction. Polym Compos 2024;45(7):5935–52. http://dx.doi.org/10.1002/pc.28171.

[11] Husseini JF, Pineda EJ, Stapleton SE. Generation of artificial 2-D fiber reinforced composite microstructures with statistically equivalent features. Composites A 2023;164:107260. http://dx.doi.org/10.1016/j.compositesa.2022.107260.

[12] Fereidouni M, Hoa SV. In-situ consolidation of thermoplastic composites by automated fiber placement: Characterization of defects. J Thermoplast Compos Mater 2025;38(2):471–511. http://dx.doi.org/10.1177/08927057241251837, arXiv:https://doi.org/10.1177/08927057241251837.

[13] Sommacal S, Matschinski A, Drechsler K, Compston P. Characterisation of void and fiber distribution in 3D printed carbon-fiber/PEEK using X-ray computed tomography. Composites A 2021;149:106487. http://dx.doi.org/10.1016/j.compositesa.2021.106487, URL: https://www.sciencedirect.com/science/article/pii/S1359835X21002098.

[14] Emtiaz SM, Pitto M, Šimáček P, Advani SG. Role of fiber clustering and resin bleeding on voids and evolution of fiber volume fraction for additively manufactured continuous carbon fiber thermoset composites with dual-cure resins. Composites A 2025;189:108601. http://dx.doi.org/10.1016/j.compositesa.2024.108601, URL: https://www.sciencedirect.com/science/article/pii/S1359835X24005992.

[15] Zhang D, Heider D, GillespieJr JW. Determination of void statistics and statistical representative volume elements in carbon fiber-reinforced thermoplastic prepregs. J Thermoplast Compos Mater 2017;30(8):1103–19. http://dx.doi.org/10.1177/0892705715618002, arXiv:https://doi.org/10.1177/0892705715618002.

[16] Gomarasca S, Peeters D, Atli-Veltin B, Dransfeld C. Characterising microstructural organisation in unidirectional composites. Compos Sci Technol 2021;215:109030. http://dx.doi.org/10.1016/j.compscitech.2021.109030, URL: https://linkinghub.elsevier.com/retrieve/pii/S0266353821003869.

[17] Breite C, Melnikov A, Turon A, de Morais A, Le Bourlot C, Maire E, Schöberl E, Otero F, Mesquita F, Costa J, Mayugo JA, Gorbatikh L, McCartney LN, Hajikazemi M, Mehdikhani M, Mavrogordato MN, Tavares R, Spearing SM, Lomov SV, Pimenta S, Van Paepegem W, Swolfs Y. Detailed experimental validation and benchmarking of six models for longitudinal tensile failure of unidirectional composites. Compos Struct 2022;279:114828. http://dx.doi.org/10.1016/j.compstruct.2021.114828, URL: https://www.sciencedirect.com/science/article/pii/S026382232101271X.

[18] Vallmajó O, Arteiro A, Guerrero J, Melro A, Pupurs A, Turon A. Micromechanical analysis of composite materials considering material variability and microvoids. Int J Mech Sci 2024;263:108781. http://dx.doi.org/10.1016/j.ijmecsci.2023.108781, URL: https://linkinghub.elsevier.com/retrieve/pii/S0020740323006835.

[19] Yang N, Zou Z, Soutis C, Potluri P, Katnam KB. Effect of micro-scale fibre uncertainties on the mechanical behaviour of natural/synthetic hybrid fibre composites. Composites A 2025;188:108570. http://dx.doi.org/10.1016/j.compositesa.2024.108570, URL: https://linkinghub.elsevier.com/retrieve/pii/S1359835X24005682.

[20] Sharma BN, Naragani D, Nguyen BN, Tucker CL, Sangid MD. Uncertainty quantification of fiber orientation distribution measurements for long-fiber-reinforced thermoplastic composites. J Compos Mater 2018;52(13):1781–97. http://dx.doi.org/10.1177/0021998317733533, URL: https://journals.sagepub.com/doi/10.1177/0021998317733533.

[21] Jeppesen N, Dahl VA, Christensen AN, Dahl AB, Mikkelsen LP. Characterization of the fiber orientations in non-crimp glass fiber reinforced composites using structure tensor. IOP Conf Ser: Mater Sci Eng 2020;942(1):012037. http://dx.doi.org/10.1088/1757-899X/942/1/012037, URL: https://iopscience.iop.org/article/10.1088/1757-899X/942/1/012037.

[22] Jeppesen N, Mikkelsen L, Dahl A, Christensen A, Dahl V. Quantifying effects of manufacturing methods on fiber orientation in unidirectional composites using structure tensor analysis. Composites A 2021;149:106541. http://dx.doi.org/10.1016/j.compositesa.2021.106541, URL: https://linkinghub.elsevier.com/retrieve/pii/S1359835X21002633.

[23] Kratz J, Galvez-Hernandez P, Pickard LR, Belnoue J, Potter K. Lab-based in-situ micro-CT observation of gaps in prepreg laminates during consolidation and cure. Composites A 2021;140:106180. http://dx.doi.org/10.1016/j.compositesa.2020.106180.

[24] Pathan M, Tagarielli V, Patsias S, Baiz-Villafranca P. A new algorithm to generate representative volume elements of composites with cylindrical or spherical fillers. Composites B 2017;110:267–78. http://dx.doi.org/10.1016/j.compositesb.2016.10.078, URL: https://linkinghub.elsevier.com/retrieve/pii/S1359836816313725.

[25] Herráez M, Segurado J, González C, Lopes C. A microstructures generation tool for virtual ply property screening of hybrid composites with high volume fractions of non-circular fibers – VIPER. Composites A 2020;129:105691. http://dx.doi.org/10.1016/j.compositesa.2019.105691, URL: https://linkinghub.elsevier.com/retrieve/pii/S1359835X19304403.

[26] Ding Y, Camanho P, Silva A. Comparison of three algorithms generating virtual microstructures in terms of the degree of randomness. Composites A 2024;177:107959. http://dx.doi.org/10.1016/j.compositesa.2023.107959.

[27] Guo R, Alves M, Mehdikhani M, Breite C, Swolfs Y. Synthesising realistic 2D microstructures of unidirectional fibre-reinforced composites with a generative adversarial network. Compos Sci Technol 2024;250:110539. http://dx.doi.org/10.1016/j.compscitech.2024.110539.

[28] Ghayoor H, Marsden CC, Hoa SV, Melro AR. Numerical analysis of resin-rich areas and their effects on failure initiation of composites. Composites A 2019;117:125–33. http://dx.doi.org/10.1016/j.compositesa.2018.11.016.

[29] Zhuang L, Pupurs A, Varna J, Talreja R, Ayadi Z. Effects of inter-fiber spacing on fiber-matrix debond crack growth in unidirectional composites under transverse loading. Composites A 2018;109:463–71. http://dx.doi.org/10.1016/j.compositesa.2018.03.031.

[30] Mortensen U, Rasmussen S, Mikkelsen L, Fraisse A, Andersen T. The impact of the fiber volume fraction on the fatigue performance of glass fiber composites. Composites A 2023;169:107493. http://dx.doi.org/10.1016/j.compositesa.2023.107493, URL: https://linkinghub.elsevier.com/retrieve/pii/S1359835X23000696.

[31] Raja MA, Lim SH, Jeon D, Bae S, Oh W, Yang I, Kang D, Ha J, Lee HE, Oh I-K, Kim S, Kim SS. Thin, uniform, and highly packed multifunctional structural carbon fiber composite battery lamina informed by solid polymer electrolyte cure kinetics. ACS Appl Mater Interfaces 2024;16(43):59128–42. http://dx.doi.org/10.1021/acsami.4c08698, URL: https://pubs.acs.org/doi/10.1021/acsami.4c08698. Publisher: American Chemical Society (ACS).

[32] Dong J, Kandemir A, Hamerton I. Microstructural characterisation of fibre-hybrid polymer composites using U-net on optical images. Composites A 2025;190:108569. http://dx.doi.org/10.1016/j.compositesa.2024.108569, URL: https://linkinghub.elsevier.com/retrieve/pii/S1359835X24005670.

[33] Jean JG, Broggi G, Caglar B. An image-based deep learning framework for flow field prediction in arbitrary-sized fibrous microstructures. Composites A 2026;200:109337. http://dx.doi.org/10.1016/j.compositesa.2025.109337.

[34] Guild F, Summerscales J. Microstructural image analysis applied to fibre composite materials: a review. Composites 1993;24(5):383–93. http://dx.doi.org/10.1016/0010-4361(93)90246-5, URL: https://linkinghub.elsevier.com/retrieve/pii/0010436193902465.

[35] Emerson MJ, Jespersen KM, Dahl AB, Conradsen K, Mikkelsen LP. Individual fibre segmentation from 3D X-ray computed tomography for characterising the fibre orientation in unidirectional composite materials. Composites A 2017;97:83–92. http://dx.doi.org/10.1016/j.compositesa.2016.12.028, URL: https://linkinghub.elsevier.com/retrieve/pii/S1359835X16304560.

[36] Naresh K, Khan K, Umer R, Cantwell W. The use of X-ray computed tomography for design and process modeling of aerospace composites: A review. Mater Des 2020;190:108553. http://dx.doi.org/10.1016/j.matdes.2020.108553, URL: https://linkinghub.elsevier.com/retrieve/pii/S0264127520300861.

[37] Gao Y, Hu W, Xin S, Sun L. A review of applications of CT imaging on fiber reinforced composites. J Compos Mater 2022;56(1):133–64. http://dx.doi.org/10.1177/00219983211050705, URL: https://journals.sagepub.com/doi/10.1177/00219983211050705.

[38] Gomarasca S, Peeters D, Atli-Veltin B, Slange T, Ratouit G, Dransfeld C. Characterising pore networks and their interrelation with the fibre architecture in unidirectional composites. Composites A 2025;190:108669. http://dx.doi.org/10.1016/j.compositesa.2024.108669, URL: https://linkinghub.elsevier.com/retrieve/pii/S1359835X24006675.

[39] Boos B, Queck C, Gurka M. High resolution – large field-of-view 3D imaging of fiber-reinforced composites with complex microstructure: stitching of lab-CT scans with single fiber resolution. Methods Microsc 2025. http://dx.doi.org/10.1515/mim-2025-0004, URL: https://www.degruyterbrill.com/document/doi/10.1515/mim-2025-0004/html.

[40] Mesquita F, Bucknell S, Leray Y, Lomov SV, Swolfs Y. Single carbon and glass fibre properties characterised using large data sets obtained through automated single fibre tensile testing. Composites A 2021;145:106389. http://dx.doi.org/10.1016/j.compositesa.2021.106389, URL: https://www.sciencedirect.com/science/article/pii/S1359835X21001135.

[41] Yuksel O, Hartley R, Broggi G, Maes V, Gomarasca S, Baumard T, Le Reun A, Lévy A, Dransfeld C, Caglard B, Kratz J. Microstructural analysis of unidirectional composites: a comparison of data reduction schemes. In: 21st European conference on composite materials. ECCM21, vol. 8, Nantes, France; 2024, p. 1397–404. http://dx.doi.org/10.60691/yj56-np80, URL: https://hal.science/hal-04746529.

[42] Broggi G, Yuksel O, Hartley R, Maes V, Kratz J, Caglar B. A multimodal fiber reinforced polymer composite micrograph dataset for image-based analysis benchmark. 2026, http://dx.doi.org/10.5281/ZENODO.17186136, URL: https://zenodo.org/doi/10.5281/zenodo.17186136.

[43] Broggi G, Yuksel O, Hartley R, Maes V, Kratz J, Caglar B. Companion website and repository for: benchmarking and sensitivity analysis of segmentation methods for image-based fiber detection in composites. 2026, http://dx.doi.org/10.5281/ZENODO.21429974, URL: https://zenodo.org/doi/10.5281/zenodo.21429974.

[44] Schindelin J, Arganda-Carreras I, Frise E, Kaynig V, Longair M, Pietzsch T, Preibisch S, Rueden C, Saalfeld S, Schmid B, Tinevez J-Y, White DJ, Hartenstein V, Eliceiri K, Tomancak P, Cardona A. Fiji: an open-source platform for biological-image analysis. Nature Methods 2012;9(7):676–82. http://dx.doi.org/10.1038/nmeth.2019, URL: https://www.nature.com/articles/nmeth.2019. Publisher: Springer Science and Business Media LLC.

[45] Vélez-García G, Wapperom P, Kunc V, Baird D, Zink-Sharp A. Sample preparation and image acquisition using optical-reflective microscopy in the measurement of fiber orientation in thermoplastic composites. J Microsc 2012;248(1):23–33. http://dx.doi.org/10.1111/j.1365-2818.2012.03646.x, URL: https://onlinelibrary.wiley.com/doi/10.1111/j.1365-2818.2012.03646.x.

[46] Studio encoding parameters of digital television for standard 4:3 and wide screen 16:9 aspect ratios. ITU-R BT.601-7, International Telecommunication Union; 2011, URL: https://www.itu.int/rec/R-REC-BT.601-7-201103-I/en.

[47] Murray A, van Kemenade H, wiredfool, Clark JA, Karpinsky A, Baranovič O, Gohlke C, Yay295, Dufresne J, Brett M, DWesl, Schmidt D, Kopachev K, Houghton A, REDxEYE, Mani S, Landey S, Koskela A, Keith-Magee R, Ware J, vashek, Piolie, T S, Douglas J, Martinez U, Caro D, Kossouho S. Python-pillow/pillow: 11.1.0. 2025, http://dx.doi.org/10.5281/ZENODO.14586647, URL: https://zenodo.org/doi/10.5281/zenodo.14586647.

[48] Lamprecht MR, Sabatini DM, Carpenter AE. CellProfiler™: Free, versatile software for automated biological image analysis. BioTechniques 2007;42(1):71–5. http://dx.doi.org/10.2144/000112257, URL: https://www.tandfonline.com/doi/full/10.2144/000112257.

[49] Smith K, Li Y, Piccinini F, Csucs G, Balazs C, Bevilacqua A, Horvath P. CIDRE: an illumination-correction method for optical microscopy. Nature Methods 2015;12(5):404–6. http://dx.doi.org/10.1038/nmeth.3323, URL: https://www.nature.com/articles/nmeth.3323.

[50] Peng T, Thorn K, Schroeder T, Wang L, Theis FJ, Marr C, Navab N. A baSiC tool for background and shading correction of optical microscopy images. Nat Commun 2017;8(1):14836. http://dx.doi.org/10.1038/ncomms14836, URL: https://www.nature.com/articles/ncomms14836.

[51] Kohli A, Angelopoulos AN, McAllister D, Whang E, You S, Yanny K, Gasparoli FM, Chang B-J, Fiolka R, Waller L. Ring deconvolution microscopy: exploiting symmetry for efficient spatially varying aberration correction. Nature Methods 2025;22(6):1311–20. http://dx.doi.org/10.1038/s41592-025-02684-5, URL: https://www.nature.com/articles/s41592-025-02684-5.

[52] Atherton T, Kerbyson D. Size invariant circle detection. Image Vis Comput 1999;17(11):795–803. http://dx.doi.org/10.1016/S0262-8856(98)00160-7, URL: https://www.sciencedirect.com/science/article/pii/S0262885698001607.

[53] Arganda-Carreras I, Kaynig V, Rueden C, Eliceiri KW, Schindelin J, Cardona A, Sebastian Seung H. Trainable weka segmentation: a machine learning tool for microscopy pixel classification. In: Murphy R, editor. Bioinformatics 2017;33(15):2424–6. http://dx.doi.org/10.1093/bioinformatics/btx180, URL: https://academic.oup.com/bioinformatics/article/33/15/2424/3092362.

[54] Niblack W. An introduction to digital image processing. Nachdr ed. Englewood Cliffs, NJ: Prentice Hall International; 1988.

[55] Dahl VA, Emerson MJ, Trinderup CH, Dahl AB. Content-based propagation of user markings for interactive segmentation of patterned images. In: 2020 IEEE/CVF conference on computer vision and pattern recognition workshops. CVPRW, Seattle, WA, USA: IEEE; 2020, p. 4280–8. http://dx.doi.org/10.1109/CVPRW50498.2020.00505, URL: https://ieeexplore.ieee.org/document/9150995/.

[56] Sanei SHR, Barsotti EJ, Leonhardt D, FertigIII RS. Characterization, synthetic generation, and statistical equivalence of composite microstructures. J Compos Mater 2017;51(13):1817–29. http://dx.doi.org/10.1177/0021998316662133, arXiv:https://doi.org/10.1177/0021998316662133.

[57] Van Der Walt S, Schönberger JL, Nunez-Iglesias J, Boulogne F, Warner JD, Yager N, Gouillart E, Yu T. Scikit-image: image processing in python. PeerJ 2014;2:e453. http://dx.doi.org/10.7717/peerj.453, URL: https://peerj.com/articles/453.

[58] Guo R, Stubbe J, Zhang Y, Schlepütz CM, Gomez CR, Mehdikhani M, Breite C, Swolfs Y, Villanueva-Perez P. Deep-learning image enhancement and fibre segmentation from time-resolved computed tomography of fibre-reinforced composites. Compos Sci Technol 2023;244:110278. http://dx.doi.org/10.1016/j.compscitech.2023.110278, URL: https://linkinghub.elsevier.com/retrieve/pii/S026635382300372X.

[59] Legland D, Arganda-Carreras I, Andrey P. MorphoLibJ: integrated library and plugins for mathematical morphology with imagej. Bioinformatics 2016;32(22):3532–4. http://dx.doi.org/10.1093/bioinformatics/btw413, URL: https://academic.oup.com/bioinformatics/article/32/22/3532/2525592.

[60] Ershov D, Phan M-S, Pylvänäinen JW, Rigaud SU, Le Blanc L, Charles-Orszag A, Conway JRW, Laine RF, Roy NH, Bonazzi D, Duménil G, Jacquemet G, Tinevez J-Y. TrackMate 7: integrating state-of-the-art segmentation algorithms into tracking pipelines. Nature Methods 2022;19(7):829–32. http://dx.doi.org/10.1038/s41592-022-01507-1, URL: https://www.nature.com/articles/s41592-022-01507-1.

[61] Chaudhury KN, Dabhade SD. Fast and provably accurate bilateral filtering. 2016, http://dx.doi.org/10.48550/ARXIV.1603.08109, URL: https://arxiv.org/abs/1603.08109. Publisher: arXiv Version Number: 1.

[62] Landini G, Randell D, Fouad S, Galton A. Automatic thresholding from the gradients of region boundaries. J Microsc 2017;265(2):185–95. http://dx.doi.org/10.1111/jmi.12474, URL: https://onlinelibrary.wiley.com/doi/10.1111/jmi.12474.

[63] Couprie M, Najman L, Bertrand G. Algorithms for the topological watershed. In: Andres E, Damiand G, Lienhardt P, editors. Discrete geometry for computer imagery. Berlin, Heidelberg: Springer Berlin Heidelberg; 2005, p. 172–82.

[64] Yang J, Rahardja S, Fränti P. Mean-shift outlier detection and filtering. Pattern Recognit 2021;115:107874. http://dx.doi.org/10.1016/j.patcog.2021.107874, URL: https://www.sciencedirect.com/science/article/pii/S0031320321000613.

[65] Katuin N, Peeters DMJ, Dransfeld CA. Method for the microstructural characterisation of unidirectional composite tapes. J Compos Sci 2021;5(10):275. http://dx.doi.org/10.3390/jcs5100275, URL: https://www.mdpi.com/2504-477X/5/10/275. Number: 10 Publisher: Multidisciplinary Digital Publishing Institute.

[66] Galvez-Hernandez P, Kratz J. Annotator bias and its effect on deep learning segmentation of uncured composite micrographs. NDT & E Int 2024;144:103088. http://dx.doi.org/10.1016/j.ndteint.2024.103088, URL: https://linkinghub.elsevier.com/retrieve/pii/S0963869524000537.

[67] Voronoi G. Nouvelles applications des paramètres continus à la théorie des formes quadratiques. premier mémoire. sur quelques propriétés des formes quadratiques positives parfaites. J Reine Angew Math (Crelles J) 1908;1908(133):97–102. http://dx.doi.org/10.1515/crll.1908.133.97, URL: https://www.degruyter.com/document/doi/10.1515/crll.1908.133.97/html.

[68] Rycroft CH. VORO++: A three-dimensional voronoi cell library in C++. Chaos 2009;19(4):041111. http://dx.doi.org/10.1063/1.3215722, URL: https://pubs.aip.org/aip/cha/article/135670.

[69] Pyrz R. Correlation of microstructure variability and local stress field in two-phase materials. Mater Sci Eng: A 1994;177(1):253–9. http://dx.doi.org/10.1016/0921-5093(94)90497-9, URL: https://www.sciencedirect.com/science/article/pii/0921509394904979.

[70] Melro A, Camanho P, Pinho S. Generation of random distribution of fibres in long-fibre reinforced composites. Compos Sci Technol 2008;68(9):2092–102. http://dx.doi.org/10.1016/j.compscitech.2008.03.013, URL: https://www.sciencedirect.com/science/article/pii/S0266353808001048.

[71] Lyckegaard A, Lauridsen EM, Ludwig W, Fonda RW, Poulsen HF. On the use of laguerre tessellations for representations of 3D grain structures. Adv Eng Mater 2011;13(3):165–70. http://dx.doi.org/10.1002/adem.201000258, URL: https://onlinelibrary.wiley.com/doi/10.1002/adem.201000258.

[72] Yazdchi K, Srivastava S, Luding S. Micro–macro relations for flow through random arrays of cylinders. Composites A 2012;43(11):2007–20. http://dx.doi.org/10.1016/j.compositesa.2012.07.020, URL: https://www.sciencedirect.com/science/article/pii/S1359835X12002217.

[73] Godbole MG, Purandare R, Harshe R, Hood A, Gururaja S, Joshi M, Advani S. Influence of filament distribution on transverse tow permeability: Model predictions and experimental validation. Composites A 2019;118:150–61. http://dx.doi.org/10.1016/j.compositesa.2018.12.024, URL: https://www.sciencedirect.com/science/article/pii/S1359835X18305001.

[74] Arteiro A, Catalanotti G, Reinoso J, Linde P, Camanho PP. Simulation of the mechanical response of thin-ply composites: From computational micro-mechanics to structural analysis. Arch Comput Methods Eng 2019;26(5):1445–87. http://dx.doi.org/10.1007/s11831-018-9291-2, URL: https://doi.org/10.1007/s11831-018-9291-2.

[75] Elnekhaily SA, Zhuang L, Talreja R. Formation of transverse cracks in cross ply laminates in an environment of nonuniformly distributed fibers. Compos Sci Technol 2024;253:110651. http://dx.doi.org/10.1016/j.compscitech.2024.110651, URL: https://www.sciencedirect.com/science/article/pii/S0266353824002215.

[76] Romanov V, Lomov SV, Swolfs Y, Orlova S, Gorbatikh L, Verpoest I. Statistical analysis of real and simulated fibre arrangements in unidirectional composites. Compos Sci Technol 2013;87:126–34. http://dx.doi.org/10.1016/j.compscitech.2013.07.030, URL: https://www.sciencedirect.com/science/article/pii/S0266353813003047.

[77] Mesquita F, Bucknell S, Leray Y, Lomov SV, Swolfs Y. Large datasets of single carbon and glass fibre mechanical properties obtained with automated testing equipment. Data Brief 2021;36:107085. http://dx.doi.org/10.1016/j.dib.2021.107085, URL: https://linkinghub.elsevier.com/retrieve/pii/S2352340921003693. Publisher: Elsevier BV.

[78] Islam F, Joannès S, Bucknell S, Leray Y, Bunsell A, Laiarinandrasana L. Investigation of tensile strength and dimensional variation of T700 carbon fibres using an improved experimental setup. J Reinf Plast Compos 2020;39(3–4):144–62. http://dx.doi.org/10.1177/0731684419873712, URL: https://journals.sagepub.com/doi/10.1177/0731684419873712.

[79] Savvas D, Stefanou G, Papadrakakis M. Determination of RVE size for random composites with local volume fraction variation. Comput Methods Appl Mech Engrg 2016;305:340–58. http://dx.doi.org/10.1016/j.cma.2016.03.002, URL: https://linkinghub.elsevier.com/retrieve/pii/S0045782516300822.

[80] Lesimple G, Iliopoulos I, Miquelard-Garnier G, Benethuiliere T, Bizet S, Fayolle B. Anomalous hydraulic fluid absorption by carbon fiber/ PEKK composites: Physical and mechanical aspects. Polym Compos 2024;45(12):10788–98. http://dx.doi.org/10.1002/pc.28507, URL: https://4spepublications.onlinelibrary.wiley.com/doi/10.1002/pc.28507.

[81] Arbter R, Beraud JM, Binetruy C, Bizet L, Bréard J, Comas-Cardona S, Demaria C, Endruweit A, Ermanni P, Gommer F, Hasanovic S, Henrat P, Klunker F, Laine B, Lavanchy S, Lomov SV, Long A, Michaud V, Morren G, Ruiz E, Sol H, Trochu F, Verleye B, Wietgrefe M, Wu W, Ziegmann G. Experimental determination of the permeability of textiles: A benchmark exercise. Composites A 2011;42(9):1157–68. http://dx.doi.org/10.1016/j.compositesa.2011.04.021, URL: https://www.sciencedirect.com/science/article/pii/S1359835X11001357.

[82] Vernet N, Ruiz E, Advani S, Alms JB, Aubert M, Barburski M, Barari B, Beraud JM, Berg DC, Correia N, Danzi M, Delavière T, Dickert M, Di Fratta C, Endruweit A, Ermanni P, Francucci G, Garcia JA, George A, Hahn C, Klunker F, Lomov SV, Long A, Louis B, Maldonado J, Meier R, Michaud V, Perrin H, Pillai K, Rodriguez E, Trochu F, Verheyden S, Wietgrefe M, Xiong W, Zaremba S, Ziegmann G. Experimental determination of the permeability of engineering textiles: Benchmark II. Composites A 2014;61:172–84. http://dx.doi.org/10.1016/j.compositesa.2014.02.010, URL: https://www.sciencedirect.com/science/article/pii/S1359835X14000505.

[83] Syerko E, Schmidt T, May D, Binetruy C, Advani S, Lomov S, Silva L, Abaimov S, Aissa N, Akhatov I, Ali M, Asiaban N, Broggi G, Bruchon J, Caglar B, Digonnet H, Dittmann J, Drapier S, Endruweit A, Guilloux A, Kandinskii R, Leygue A, Mahato B, Martínez-Lera P, Matveev M, Michaud V, Middendorf P, Moulin N, Orgéas L, Park C, Rief S, Rouhi M, Sergeichev I, Shakoor M, Shishkina O, Swolfs Y, Tahani M, Umer R, Vanclooster K, Vorobyev R. Benchmark exercise on image-based permeability determination of engineering textiles: Microscale predictions. Composites A 2023;167:107397. http://dx.doi.org/10.1016/j.compositesa.2022.107397, URL: https://linkinghub.elsevier.com/retrieve/pii/S1359835X22005784.

[84] May D, Advani S, Duhovic M, Endruweit A, Fauster E, George A, Liotier P-J, Lira C, Lomov S, Pucci M, Schmeer S, Abliz D, Berg D, Binetruy C, Bodaghi M, Comas-Cardona S, Etchells M, Govignon Q, Koorevaar A, Michaud V, Park C, Schubnel R, Sousa P, Ravel R, Rouhi M, Syerko E, Umer R, Vollmer M, Yong A. A new ISO standard for the experimental characterization of in-plane permeability of fibrous reinforcements. Composites A 2025;190:108592. http://dx.doi.org/10.1016/j.compositesa.2024.108592, URL: https://linkinghub.elsevier.com/retrieve/pii/S1359835X24005906.

[85] Yong AXH, Endruweit A, George A, May D, Aksoy YA, Ali MA, Allen T, Baral P, Betteridge C, Brauner C, Caglar B, Chiminelli A, Cracknell D, Dame L, Dittmann J, Dransfeld C, Drapier S, García Manrique JA, Garrigou E, Guilloux A, Hubert P, Ivens J, Janzen J, Khan T, Kikuta H, Kind K, Laspalas M, Lee J, Liu X, Lizaranzu M, Lomov SV, Masania K, Michaud V, Middendorf P, Miguel S, Muñoz J, Narayana SS, Park CH, Pedoto G, Pisupati A, Sayinbas D, Sousa P, Sozer M, Staal J, Steinhardt M, Teixido H, Umer R, Vincent JD, Werlen V, Yuksel O. Towards standardisation of the out-of-plane permeability measurement for reinforcement textiles. Composites A 2025;190:108630. http://dx.doi.org/10.1016/j.compositesa.2024.108630, URL: https://www.sciencedirect.com/science/article/pii/S1359835X24006286.

[86] Fazlali B, Breite C, Czél G, Fiedler B, Gibhardt D, Hojo M, Koerber H, Kumar R, Velasco ML, McEnteggart I, Mikkelsen LP, Paris F, Taketa I, Wisnom MR, Swolfs Y. Round-robin programme for longitudinal tensile testing of unidirectional composites: results, conclusions, and recommendations. Polym Test 2025;108974. http://dx.doi.org/10.1016/j.polymertesting.2025.108974, URL: https://www.sciencedirect.com/science/article/pii/S0142941825002880.

[87] Lavaggi T, Gillespie JW, Mulye PD, Binetruy C, Advani SG. Influence of sample size on permeability of carbon–carbon composites with stochastic microstructure. Composites A 2025;198:109126. http://dx.doi.org/10.1016/j.compositesa.2025.109126, URL: https://www.sciencedirect.com/science/article/pii/S1359835X25004208.

[88] Crameri F. Scientific colour maps. 2023, http://dx.doi.org/10.5281/ZENODO.1243862, URL: https://zenodo.org/record/1243862.